

# Quantum Dynamics Simulations of the 2D Spectroscopy for Exciton Polaritons

M. Elious Mondal,<sup>1, a)</sup> Eric Koessler,<sup>1</sup> Justin Provazza,<sup>2</sup> A. Nickolas Vamivakas,<sup>3, 4</sup> Steven T. Cundiff,<sup>5</sup> Todd D. Krauss,<sup>1, 3, b)</sup> and Pengfei Huo<sup>1, 3, c)</sup>

<sup>1)</sup> *Department of Chemistry, University of Rochester, Rochester, New York, 14627, USA*

<sup>2)</sup> *Quantum Simulation Technologies, Inc., Boston, MA 02135, USA*

<sup>3)</sup> *The Institute of Optics, Hajim School of Engineering, University of Rochester, Rochester, NY 14627, USA*

<sup>4)</sup> *Department of Physics and Astronomy, University of Rochester, Rochester, NY 14627, USA*

<sup>5)</sup> *Department of Physics, University of Michigan, Ann Arbor, MI 48109, USA*

We develop an accurate and numerically efficient non-adiabatic path-integral approach to simulate the non-linear spectroscopy of exciton-polariton systems. This approach is based on the partial linearized density matrix (PLDM) approach to model the exciton dynamics with an explicit propagation of the phonon bath environment, combined with a stochastic Lindblad dynamics approach to model the cavity loss dynamics. Through simulating both linear and polariton 2-dimensional electronic spectra (2DES), we systematically investigate how light-matter coupling strength and cavity loss rate influence the optical response signal. Our results confirm the polaron decoupling effect, which is the reduced exciton-phonon coupling among polariton states due to the strong light-matter interactions. We further demonstrate that the polariton coherence time can be significantly prolonged compared to the electronic coherence outside the cavity.

## I. INTRODUCTION

Coupling molecular excitations to a quantized radiation field inside an optical cavity produces a set of light-matter hybrid states known as polaritons. These polariton states, which are a hybridization of matter excitation and photonic excitation, have shown great promise in changing the reactivities of molecules<sup>1–5</sup>. In particular, the light-matter interaction has been shown to effectively reduce the coupling between excitons and phonons, which is commonly referred to as the polaron decoupling effect.<sup>6,7</sup> This polaron decoupling effect results in an enhanced charge transfer rate constant,<sup>6</sup> reduction of the homogeneous linewidth of spectra,<sup>8,9</sup> and causes ballistic exciton-polariton transport.<sup>10–12</sup> In particular, the exciton-polariton coherence lifetime should be prolonged due to reduced coupling with the phonon bath.<sup>9</sup>

Linear<sup>13</sup> and non-linear spectroscopy<sup>9,14,15</sup> are powerful measurements that provide a fundamental understanding of the photophysics of polariton systems. Recent theoretical progress<sup>16–18</sup> has focused on simulating the polariton 2-dimensional electronic spectra (2DES) spectra, such as an analytic expression based on the non-Hermitian Hamiltonian,<sup>17</sup> or based on the Heisenberg-Langevin equation.<sup>18</sup> Nevertheless, there is a lack of general theoretical approaches that can accurately simulate exciton-polariton spectra beyond perturbative methods,<sup>18</sup> with an accurate description of the non-Markovian exciton-phonon coupling and the cavity loss dynamics.

In this paper, we combine the partial linearized density

matrix (PLDM) approach<sup>19–22</sup> with a stochastic Lindblad dynamics to simulate polaritonic spectroscopy in lossy cavities. To include the cavity loss dynamics, we develop stochastic Lindblad dynamics, which exactly reproduce the Lindblad dynamics when averaged over an ensemble of trajectories. With this combined approach, we simulate the linear and non-linear spectra of a monomer and dimer coupled to a single-mode cavity. With simulated linear and 2DES spectra of the polariton, we systematically investigated the influence of the light-matter coupling strength and cavity loss rate on the optical signals. In particular, we demonstrate that the polariton coherence (interpreted from the off-diagonal peak of the 2DES spectra) can be significantly prolonged by increasing the light-matter coupling strength, providing a theoretical verification of the polaron decoupling effect.<sup>9</sup>

## II. THEORY AND METHOD

In this section, we provide a brief overview of linear and non-linear spectroscopy using the Liouville pathways that contribute to the response signals. We then briefly review how the PLDM approach computes response functions for any operator dynamics. We further use Lindblad dynamics to describe the effect of cavity loss and develop a new trajectory-based approach to combine Lindblad dynamics with the PLDM approach, in order to provide a systematic way to incorporate cavity loss in polariton dynamics simulations for calculating linear and non-linear spectra.

<sup>a)</sup> Electronic mail: mmondal@ur.rochester.edu

<sup>b)</sup> Electronic mail: todd.krauss@rochester.edu

<sup>c)</sup> Electronic mail: pengfei.huo@rochester.edu

### A. Linear and Non-linear spectroscopy

The linear absorption can be written as a dipole-dipole auto-correlation function with the ensemble averaging done over the ground state density matrix of the ensemble.<sup>23</sup> For linear absorption spectroscopy, the laser strength is much weaker than the internal interaction energies of the system such that we can treat it as a perturbation. The linear response of a system to the external radiation field, in the impulsive limit, is expressed as

$$R^{(1)}(t_1) = -i\text{Tr}[\hat{\mu}(t_1)[\hat{\mu}(t_0), \hat{\rho}^{(g)}]]. \quad (1)$$

where  $t_0$  is the time of interaction between the first laser and the system, where  $t_1$  is the time when the system emits the response signal. Further,  $\hat{\mu}(t_1)$  is the dipole operator in the interaction picture,  $\hat{\rho}^{(g)}$  represents the initial density matrix of the system in the equilibrium ground state at  $t = -\infty$ , ( $\hat{\rho}^{(g)} = \hat{\rho}(-\infty)$ ). The frequency domain spectra can be computed from a smoothed Fourier transform of  $R^{(1)}(t)$  as follows

$$R^{(1)}(\omega) = \int_0^T R^{(1)}(t) e^{i\omega t} \cos\left(\frac{\pi t}{2T}\right) dt, \quad (2)$$

where  $T$  is the maximum time of the recorded time-domain spectra and  $\cos(\pi t/2T)$  is a smoothing function. The linear spectra are often limited in the amount of information that can be extracted for a given system, such as its inability to distinguish different broadening mechanisms arising due to homogeneous or inhomogeneous distributions of frequencies.

Non-linear spectroscopy, on the other hand, provides much more detailed information that is not available in linear spectra.<sup>23-30</sup> More detailed dynamical information can be extracted (compared to the linear spectra) by perturbing the system multiple times with consecutive laser pulses. Each additional laser pulse adds a higher-order non-linear perturbation to the overall density matrix, which can be interpreted from a specific pathway in the Liouville space. For a general two-dimensional spectroscopy experiment, three laser pulses are used with different time delays and thus, in the impulsive limit, the 3<sup>rd</sup> order response can be calculated from a four-point correlation function

$$R^{(3)}(t_1, t_2, t_3) = -i\text{Tr}[\hat{\mu}(t_3)[\hat{\mu}(t_2), [\hat{\mu}(t_1), [\hat{\mu}(t_0), \hat{\rho}^{(g)}]]]]. \quad (3)$$

Here, the factor of  $-i$  comes from  $(-i)^3$  in the third order of perturbative expansion. Here,  $t_1$  and  $t_2$  are the time of interaction between the system and the second and third laser pulses, respectively, whereas  $t_4$  is the time at which the system produces the non-linear response signal. Further,  $R^{(3)}$  can be decomposed into 8 different Liouville pathways, each representing a separate Feynman diagram and giving rise to a non-linear response signal. Each of the response signals is also accompanied by a phase factor that makes it possible to have an independent spatial direction of detection for each diagram.

These Liouville pathways (Feynman diagrams) can be categorized as either rephasing or non-rephasing signals, based on the phase accumulated by the signal after the application of the third laser pulse. These signals can be further partitioned into three physical processes, namely, stimulated emission (SE), ground-state bleaching (GSB), and excited-state absorption (ESA). For notation purposes, we only write the first four Liouville pathways in Eq. 4a - Eq. 4d

$$R_1^{(3)}(t_1, t_2, t_3) = -i\text{Tr}[\hat{\mu}(t_3)\hat{\mu}(t_0)\hat{\rho}^{(g)}\hat{\mu}(t_1)\hat{\mu}(t_2)], \quad (4a)$$

$$R_2^{(3)}(t_1, t_2, t_3) = -i\text{Tr}[\hat{\mu}(t_3)\hat{\mu}(t_1)\hat{\rho}^{(g)}\hat{\mu}(t_0)\hat{\mu}(t_2)], \quad (4b)$$

$$R_3^{(3)}(t_1, t_2, t_3) = -i\text{Tr}[\hat{\mu}(t_3)\hat{\mu}(t_2)\hat{\rho}^{(g)}\hat{\mu}(t_0)\hat{\mu}(t_1)], \quad (4c)$$

$$R_4^{(3)}(t_1, t_2, t_3) = -i\text{Tr}[\hat{\mu}(t_3)\hat{\mu}(t_2)\hat{\mu}(t_1)\hat{\mu}(t_0)\hat{\rho}^{(g)}], \quad (4d)$$

while the remaining four pathways are just the complex conjugates of the listed four (which can be verified by expanding Eq. 3 and using the cyclic property of the trace of matrix multiplications).

In purely-absorptive 2D experiments, the signal is calculated by adding the rephasing and non-rephasing signals as follows

$$R_{\text{rep}}^{(3)}(t_1, t_2, t_3) = R_2^{(3)} + R_3^{(3)} + R_1^{(3)*}, \quad (5a)$$

$$R_{\text{nrp}}^{(3)}(t_1, t_2, t_3) = R_1^{(3)} + R_4^{(3)} + R_2^{(3)*}. \quad (5b)$$

In Eq. 5a and Eq. 5b, we arrange the terms on the right-hand side in the order of SE, GSB, and ESA, respectively. Note that the formalism we present below can be used to calculate all possible non-linear spectroscopy experiments and is not limited to just Eq. 5a and Eq. 5b. Usually, 2D spectra are represented as the imaginary part of a  $t_2$  varying series of Fourier transformed  $t_1$  and  $t_3$  axes. Because of the rephasing and non-rephasing, the signals are generated in different quadrants of the frequency domain. As such, the 2D Fourier transform is calculated by

$$R_{\text{rep}}^{(3)}(\omega_1, t_2, \omega_3) = \int_0^{T_1} \int_0^{T_3} R_{\text{rep}}^{(3)} e^{i\omega_3 t_3 - i\omega_1 t_1} S_1 S_3 dt_1 dt_3, \quad (6a)$$

$$R_{\text{nrp}}^{(3)}(\omega_1, t_2, \omega_3) = \int_0^{T_1} \int_0^{T_3} R_{\text{nrp}}^{(3)} e^{i\omega_3 t_3 + i\omega_1 t_1} S_1 S_3 dt_1 dt_3, \quad (6b)$$

where the smoothing function  $S_i$  is

$$S_i = \cos\left(\frac{\pi t_i}{2T_i}\right).$$

With Eq. 6a and Eq. 6b, we can now represent the conventional purely-absorptive 2D spectra as

$$R^{(3)}(\omega_1, t_2, \omega_3) = -\text{Im}(R_{\text{rep}}^{(3)} + R_{\text{nrp}}^{(3)}). \quad (7)$$

## B. PLDM Approach for Dynamics Propagation

The diabatic Hamiltonian of a system under the influence of a nuclear bath can be expressed as

$$\hat{H} = \frac{\hat{P}^2}{2M} + \sum_a^{\mathcal{N}} V_{aa}(\hat{R}) |a\rangle\langle a| + \frac{1}{2} \sum_{b \neq a}^{\mathcal{N}} V_{ab}(\hat{R}) |a\rangle\langle b| \quad (8)$$

where  $\hat{R}$  and  $\hat{P}$  are the nuclear position and momenta, respectively, of the bath coordinates,  $M$  is the mass of the bath particles, and  $\{|a\rangle, |b\rangle\}$  are the quantum DOFs of the system (e.g. the electronic excitation and photonic exciton of the molecule-cavity hybrid system). As the total number of states increases, quantum dynamics simulations can become expensive due to the exponential scaling<sup>19,31–33</sup> of the calculation with the number of degrees of freedom. Over the years, there has been an enormous development of many semi-classical<sup>19,34</sup> mixed quantum-classical<sup>35–37</sup>, and quantum master equation approaches<sup>38–42</sup>, each with their own strengths and shortcomings. Quantum master equation approaches are often based on perturbative approaches which are restricted to weak system-bath couplings and often fail to account for non-Markovian effects from bath feedback to the quantum subsystem DOFs. Semi-classical approaches, on the other hand, have been shown to accurately treat non-Markovian feedback from the nuclear bath to the quantum subsystem and can accurately treat a wide range of system-bath couplings.<sup>19,34</sup>

Here, we use the PLDM approach<sup>19–22</sup> to compute optical spectra. The time evolution of the matrix element of the operator  $\hat{O}$  is given by

$$\begin{aligned} & \left\langle n_t, R_t + \frac{\Delta t}{2} \left| \hat{O}(t) \right| n'_t, R_t - \frac{\Delta t}{2} \right\rangle \quad (9) \\ & = \sum_{n_0, n'_0} \int dR_0 dP_1 dx^F dp^F dx^B dp^B O_W^{n_0 n'_0}(R_0, P_1) e^{iP_1 \Delta t} \\ & \quad \times G_0^F G_0^B \frac{1}{2} (x_{n_0}^F - ip_{n_0}^F)(x_{n'_0}^B + ip_{n'_0}^B) \\ & \quad \times \frac{1}{2} (x_{n_t}^F(t) + ip_{n_t}^F(t))(x_{n'_t}^B(t) - ip_{n'_t}^B(t)). \end{aligned}$$

In the above expression,  $x_a^F$  and  $p_a^F$  are the Meyer-Miller-Stock-Thoss (MMST) mapping variables<sup>43–45</sup> associated with the state  $|a\rangle$  for the forward propagation, and  $x_a^B$  and  $p_a^B$  are the corresponding mapping variables for the backward propagation. Furthermore,  $G_0^F = \exp\left[-\frac{1}{2} \sum_a (p_a^{F2} + x_a^{F2})\right]$  is a Gaussian function of the mapping variables, with an analogous expression<sup>19,20</sup> for  $G_0^B$ . These Gaussian terms arise due to the coherent state representation of the mapping variables used in PLDM.<sup>19–21,46</sup> Further,  $R$  and  $P$  denote the mean position of the bath and the momentum, and  $\Delta$  is the path difference between the forward and the backward nuclear paths.

The initial nuclear phase space variables are sampled from the Wigner distribution

$$O_W^{n_0 n'_0}(R_0, P_1) = \int dZ_0 \left\langle n_0, R_0 + \frac{Z_0}{2} \left| \hat{O} \right| n'_0, R_0 - \frac{Z_0}{2} \right\rangle e^{-iP_1 Z_0}. \quad (10)$$

The nuclear phase space variables  $(R, P)$  evolve according to the mean force from the forward and backward mapping variables,

$$\mathcal{F}(R) = -\frac{1}{2} \nabla_R \{ \mathcal{H}(R, \mathbf{x}^F, \mathbf{p}^F) + \mathcal{H}(R, \mathbf{x}^B, \mathbf{p}^B) \}. \quad (11)$$

With the MMST diabatic mapping, the Hamiltonian (Eq. 8) is expressed (without the zero-point energy correction) in terms of mapping variables  $(\mathbf{x}, \mathbf{p})$ ,

$$\begin{aligned} \mathcal{H}(R) & = \frac{P^2}{2M} + \frac{1}{2} \sum_a V_{aa}(R)(x_a^2 + p_a^2 - 1) \\ & \quad + \frac{1}{2} \sum_{b \neq a} V_{ab}(R)(x_a x_b + p_a p_b). \end{aligned} \quad (12)$$

To summarize, the equation of motion for the coupled electronic and nuclear DOFs is

$$\frac{\partial R}{\partial t} = P, \quad \frac{\partial P}{\partial t} = \mathcal{F}, \quad (13a)$$

$$\frac{\partial x_a}{\partial t} = \frac{\partial \mathcal{H}}{\partial p_a} = \frac{1}{\hbar} \sum_b V_{ab}(R) p_b, \quad (13b)$$

$$\frac{\partial p_a}{\partial t} = -\frac{\partial \mathcal{H}}{\partial x_a} = -\frac{1}{\hbar} \sum_b V_{ab}(R) x_b, \quad (13c)$$

where the equations of motion for the mapping variables are identical for both the forward and backward variables,  $x_a = \{x_a^F, x_a^B\}$  and  $p_a = \{p_a^F, p_a^B\}$ .

## C. $\mathcal{L}$ -PLDM (Lindblad-PLDM) Dynamics

We aim to seamlessly incorporate cavity loss dynamics with the polariton dynamics simulation using PLDM. We begin with a general discussion of the Lindblad dynamics and then develop a new trajectory-based approach that can incorporate Lindblad loss dynamics with PLDM.

The Hamiltonian  $\hat{H}$  (Eq. 8) could interact with an additional dissipative environment, such as the photonic bath (far field, non-cavity modes) that causes cavity loss. We denote the total Hamiltonian as

$$\hat{H}_T = \hat{H}_S + \hat{H}_E + \hat{H}_I, \quad (14)$$

where  $\hat{H}_E = \sum_j \hbar \omega_j (\hat{b}_j^\dagger \hat{b}_j + \frac{1}{2})$  accounts for the environmental DOF (far field, non-cavity modes), and the interactions between  $\hat{H}_S$  and  $\hat{H}_E$  through the interaction term  $\hat{H}_I = (\hat{a}^\dagger + \hat{a}) \otimes \sum_j \hbar g_j (\hat{b}_j^\dagger + \hat{b}_j)$  that accounts for the interactions between the cavity mode (see Eq. 36)

described by  $\{\hat{a}^\dagger, \hat{a}\}$  and the far-field modes  $\{\hat{b}_j^\dagger, \hat{b}_j\}$ . A detailed discussion of cavity loss (and the expression of  $\hat{H}_E$  and  $\hat{H}_I$ ) can be found in Appendix D of Ref. 47. Denoting the total density operator  $\hat{\rho}_T$  associated with the total Hamiltonian  $\hat{H}_T$ , we can trace out the environmental DOF and have the system part of the reduced density operator as

$$\hat{\rho}_S = \text{Tr}_E[\hat{\rho}_T], \quad (15)$$

as well as the reduced density operator for the quantum subsystem

$$\hat{\rho} = \text{Tr}_E \text{Tr}_R[\hat{\rho}_T] = \text{Tr}_R[\hat{\rho}_S]. \quad (16)$$

For simplicity, in the following of the paper, we denote the system part of the Hamiltonian (which includes electronic, photonic, and nuclear DOFs) as

$$\hat{H} \equiv \hat{H}_S. \quad (17)$$

In the Markovian regime of system-environment interactions, the dynamics of  $\hat{\rho}$  can be described using the Lindblad master equation

$$\frac{\partial \hat{\rho}}{\partial t} = \mathcal{L}_{\hat{H}}[\hat{\rho}] + \mathcal{L}_{\hat{L}}[\hat{\rho}], \quad (18)$$

where  $\mathcal{L}_{\hat{H}}[\hat{\rho}]$  propagates the reduced density matrix dynamics corresponding to the system Hamiltonian  $\hat{H}$  (Eq. 8). The dynamics governed by  $\mathcal{L}_{\hat{H}}[\hat{\rho}]$ , which includes the quantum subsystem, as well as interactions with non-Markovian phonons, can be simulated using PLDM using Eq. 9 and the corresponding EOMs in Eq. 13. The dissipator  $\mathcal{L}_{\hat{L}}$  accounts for the cavity loss channel causing the system to relax

$$\mathcal{L}_{\hat{L}}[\hat{\rho}] = \Gamma \left( \hat{L} \hat{\rho} \hat{L}^\dagger - \frac{1}{2} \{ \hat{L}^\dagger \hat{L}, \hat{\rho} \} \right), \quad (19)$$

where  $\Gamma$  is the rate of relaxation of the jump operator which quantifies the coupling strength of the system to the environment, and  $\{\hat{A}, \hat{B}\} = \hat{A}\hat{B} + \hat{B}\hat{A}$  is the anti-commutator. For multiple relaxation channels, each associated with a decay rate  $\Gamma_\varphi$  and jump operator  $\hat{L}_\varphi$ , Eq. 19 needs to be generalized to  $\mathcal{L}_{\hat{L}}[\hat{\rho}] = \sum_\varphi \Gamma_\varphi (\hat{L}_\varphi \hat{\rho} \hat{L}_\varphi^\dagger - \frac{1}{2} \{ \hat{L}_\varphi^\dagger \hat{L}_\varphi, \hat{\rho} \})$  for each loss channel  $\varphi$ .

In the context of the present work, we are mainly interested in jump operators that decay the population from state  $|1\rangle$  to state  $|0\rangle$ , of the form

$$\hat{L} = |0\rangle\langle 1|, \quad (20)$$

where for multiple decay channels, one should sum the dissipators of each jump operator. A detailed example of  $\hat{L}$  for describing cavity loss can be found in Eq. 43 and Eq. 44.

To incorporate Lindblad decay dynamics into the PLDM method, we develop the following approach,

which we refer to as the  $\mathcal{L}$ -PLDM method, with a similar procedure documented in the work of  $\mathcal{L}$ -MFE (Lindblad mean-field Ehrenfest) in Ref. 47. The current approach follows the original idea used in 47, of matching the exact time evolution of the density matrix governed by the Lindblad dissipator, with a deterministic change of the magnitude of the electronic expansion coefficients (in terms of mapping variables), but stochastic changes of the phases for these coefficients. The primary difference between MFE and PLDM, however, is that the PLDM method effectively uses the outer product of two separate coefficients (for forward and backward mapping variables, see Eq. 9) to calculate the estimator of the density matrix instead of a single set of coefficients in Ehrenfest dynamics. The use of two separate coefficients (associated with the forward and backward paths of mapping DOFs) allows for the possibility of populations being complex instead of purely non-negative and real. The  $\mathcal{L}$ -MFE approach does not work correctly for complex populations, and thus a modified method for PLDM must be used.

Similar to the  $\mathcal{L}$ -MFE approach, the propagation of the forward and backward variables are split into a PLDM quantum dynamics propagation step and a Lindblad decay step which can be evaluated separately.<sup>47</sup> For the Lindblad decay step, the real mapping variables at time  $t$  can be combined into complex mapping variables (coherent state variables) as follows

$$z_a^F(t) = \frac{1}{\sqrt{2}}(x_a^F(t) + ip_a^F(t)), \quad (21a)$$

$$z_a^B(t) = \frac{1}{\sqrt{2}}(x_a^B(t) + ip_a^B(t)). \quad (21b)$$

The forward and backward coefficients for state  $|a\rangle$  at time  $t$ ,  $Z_a^F(t)$  and  $Z_a^B(t)$ , based on the PLDM expression in Eq. 9 (see the 3rd line of the expression) are calculated by weighting the current complex mapping variables with the initial value of the mapping variables for the initially focused states  $n_0$  and  $n'_0$  as follows

$$Z_a^F(t) = z_a^F(t) z_{n_0}^{F*}(0), \quad (22a)$$

$$Z_a^B(t) = z_a^B(t) z_{n'_0}^{B*}(0). \quad (22b)$$

Using Eq. 22, the reduced density matrix estimator elements for the quantum subsystem  $\hat{\rho}$  at time  $t$  are given by averaging over the whole ensemble of trajectories according to the PLDM approach [c.f. Eq. 9] as follows

$$\rho_{ab}(t) = \frac{1}{N_{\text{traj}}} \sum_{\xi=1}^{N_{\text{traj}}} Z_{a,\xi}^F(t) Z_{b,\xi}^{B*}(t), \quad (23)$$

where  $N_{\text{traj}}$  is the number of trajectories and  $\xi$  is the index of a trajectory. To incorporate Lindblad decay, the time-evolved coefficients after a time step  $dt$  are written as the product of the previous coefficient times a complex random number

$$\begin{aligned} Z_{a,\xi}^F(t+dt) &= \eta_{a,\xi}^F Z_{a,\xi}^F(t), \\ Z_{a,\xi}^B(t+dt) &= \eta_{a,\xi}^B Z_{a,\xi}^B(t), \end{aligned} \quad (24)$$

where  $\{\eta\}$  are complex random numbers sampled at each time step. The time-evolved density matrix estimator can now be written as

$$\rho_{ab}(t + dt) = \frac{1}{N_{\text{traj}}} \sum_{\xi=1}^{N_{\text{traj}}} \eta_{a,\xi}^{\text{F}} \mathcal{Z}_{a,\xi}^{\text{F}}(t) \cdot \eta_{b,\xi}^{\text{B}*} \mathcal{Z}_{b,\xi}^{\text{B}*}(t). \quad (25)$$

The joint probability distribution of these random variables is chosen such that the expectation value of the propagated density matrix estimator obeys the exact time evolution of the initial density matrix estimator as follows

$$\langle \rho_{ab}(t + dt) \rangle = e^{\mathcal{L} dt} [\hat{\rho}(t)]_{ab}, \quad (26)$$

where  $\langle \rho_{ab}(t + dt) \rangle$  is the formal expectation value of the density matrix estimator element which can be calculated by integrating over the joint probability distribution of the random variables  $\{\eta\}$ . For jump operators of the form in Eq. 20, it can be shown that the following expressions of the random variables for states  $|1\rangle$  and  $|0\rangle$  satisfy Eq. 26

$$\eta_{1,\xi}^{\text{F}} = \eta_{1,\xi}^{\text{B}} = e^{-\Gamma dt/2}, \quad (27a)$$

$$\eta_{0,\xi}^{\text{F}} = \eta_{0,\xi}^{\text{B}*} = 1 + (2r - 1) \sqrt{3(1 - e^{-\Gamma dt}) \frac{\mathcal{Z}_{1,\xi}^{\text{F}}(t) \mathcal{Z}_{1,\xi}^{\text{B}*}(t)}{\mathcal{Z}_{0,\xi}^{\text{F}}(t) \mathcal{Z}_{0,\xi}^{\text{B}*}(t)}}, \quad (27b)$$

where  $r \in [0, 1]$  is a random number sampled from the standard uniform distribution at each time step for each trajectory. A brief derivation of the approach described in Eqs. 27a and 27b is provided in Appendix A. Note that while Eqs. 27a and 27b preserve the trace of the expectation value of the density matrix estimator among the ensemble of trajectories, the trace of an individual trajectory's density matrix estimator may not be conserved due to the nature of the sampling. Furthermore, unlike the  $\mathcal{L}$ -MFE approach, which has a fully deterministic change in the coefficient magnitudes, the change in the magnitude of the ground-state coefficient in Eq. 27b is stochastic, which was necessary to deal with the potential complex population estimators for each individual trajectory ( $\mathcal{Z}_{a,\xi}^{\text{F}}(t) \mathcal{Z}_{b,\xi}^{\text{B}*}(t)$  in Eq. 23) that arise in the PLDM method. The propagated forward mapping variables can be recovered as follows

$$x_{a,\xi}^{\text{F}}(t + dt) = \sqrt{2} \operatorname{Re} \left[ \frac{\mathcal{Z}_{a,\xi}^{\text{F}}(t + dt)}{z_{n_0,\xi}^{\text{F}*}(0)} \right], \quad (28a)$$

$$p_{a,\xi}^{\text{F}}(t + dt) = \sqrt{2} \operatorname{Im} \left[ \frac{\mathcal{Z}_{a,\xi}^{\text{F}}(t + dt)}{z_{n_0,\xi}^{\text{F}*}(0)} \right], \quad (28b)$$

and likewise for the backward mapping variables.

The Lindblad decay procedure described above is combined with the regular propagation of the mapping variables by PLDM. The overall propagation of the density

matrix estimator during a time step (similar to the previous work as described in Ref. 47) can thus be summarized as

$$\hat{\rho}(t + dt) = \mathcal{L}[\hat{\rho}] = e^{\mathcal{L}_L dt/2} e^{\mathcal{L}_H dt} e^{\mathcal{L}_L dt/2} \hat{\rho}(t), \quad (29)$$

where  $e^{\mathcal{L}_L}$  is the decay dynamics propagation outlined above (in Eq. 28 and Eq. 27) and  $e^{\mathcal{L}_H}$  is the PLDM propagation based on the system Hamiltonian. In the scheme of Eq. 29, we have used the symmetrized Trotter decomposition to reduce the error of using a finite  $dt$ . This stochastic approach is briefly compared to Lindblad dynamics in Appendix B.

### III. MODEL SYSTEMS

In this work, we investigate an excitonic monomer and an excitonic dimer coupled to a resonant optical cavity. The excitonic part is described by a Frenkel excitonic Hamiltonian. We perform spectroscopy simulations for both monomers and dimers placed outside and inside the cavity and compare the changes induced by coupling to the cavity.

The exciton Hamiltonian is given by

$$\hat{H}_{\text{ex}} = \sum_m (\bar{\epsilon} + \epsilon_m) |m\rangle\langle m| + \sum_{mn} J_{mn} |m\rangle\langle n|, \quad (30)$$

where  $\bar{\epsilon}$  is the reference exciton energy,  $\epsilon_m$  is the on-site excitation energy for site  $m$ , and  $J_{mn}$  is the diabatic coupling between site  $m$  and  $n$ . The diabatic states are represented in the exciton basis where  $|m\rangle \equiv |g_1, g_2, \dots, e_m, g_{m+1}, \dots, g_N\rangle$  represents the exciton localized on the  $m_{\text{th}}$  monomer

$$|m\rangle = \left( \bigotimes_{n \neq m} |g_n\rangle \right) \otimes |e_m\rangle. \quad (31)$$

Each of the individual sites has their own individual phonon bath

$$\hat{H}_{\text{R}} = \frac{1}{2} \sum_{m,\nu} \left( \hat{P}_{m,\nu}^2 + \omega_{m,\nu}^2 \hat{R}_{m,\nu}^2 \right), \quad (32)$$

where the mass for each nuclear mode is set to be  $M_\nu = 1$ . Further,  $\hat{H}_{\text{ex}}$  and  $\hat{H}_{\text{R}}$  are coupled through the exciton-phonon coupling

$$\hat{H}_{\text{ex-R}} = \sum_m \sum_\nu c_{m,\nu} \hat{R}_{m,\nu} \otimes |m\rangle\langle m|. \quad (33)$$

These coupling constants are sampled from the Debye spectral density

$$J_m(\omega) = \frac{\pi}{2} \sum_\nu \frac{c_{m,\nu}^2}{\omega_{m,\nu}} \delta(\omega - \omega_{m,\nu}) = \frac{2\lambda\omega_0\omega}{\omega_0^2 + \omega^2}, \quad (34)$$

where  $\lambda$  is the reorganization energy and  $\omega_0$  is the cutoff frequency of the bath. Here, we assume that each site

$m$  has identical phonon baths and associated spectral density.

When coupling this exciton system to a cavity, the total Hamiltonian is described at the Jaynes-Cummings (JC) level of theory as

$$\hat{H} = \hat{H}_{\text{ex}} + \hat{H}_{\text{ex-R}} + \hat{H}_{\text{R}} + \hat{H}_{\text{ph}} + \hat{H}_{\text{ex-ph}}, \quad (35)$$

where the photonic Hamiltonian is expressed as

$$\hat{H}_{\text{ph}} = \hbar\omega_c(\hat{a}^\dagger\hat{a} + \frac{1}{2}), \quad (36)$$

where  $\hat{a}^\dagger$  and  $\hat{a}$  are the creation and annihilation operators, respectively, for the cavity field. The exciton-photon interaction (due to the coupling between molecules and the cavity mode) is given by

$$\hat{H}_{\text{ex-ph}} = \sum_m \hbar g_c(m) \cdot (|G\rangle\langle m| \hat{a}^\dagger + |m\rangle\langle G| \hat{a}), \quad (37)$$

under the rotating wave approximation, and the collective ground state  $|G\rangle$  is defined as

$$|G\rangle = \bigotimes_j |g_j\rangle. \quad (38)$$

The photon-matter coupling strength is given by

$$g_c(m) = \mu_m \sqrt{\frac{\hbar\omega_c}{2\mathcal{V}\epsilon_0}}, \quad (39)$$

where  $\mathcal{V}$  is the cavity volume,  $\epsilon_0$  is the cavity permittivity, and  $\mu_m$  is the transition dipole moment associated with site  $m$ . The total dipole operator for the matter

$$\hat{\mu} = \sum_m \mu_m (|G\rangle\langle m| + |m\rangle\langle G|) \quad (40)$$

is responsible for the optical spectra. Here, we assume that the transition dipole direction always aligns with the cavity field polarization direction, and we also assume that there are no permanent dipoles. Further, we introduce the following short-hand notation for the exciton-Fock state

$$|G, k\rangle \equiv |G\rangle \otimes |k\rangle, \quad |m, k'\rangle \equiv |m\rangle \otimes |k'\rangle, \quad (41)$$

where  $|k\rangle$  and  $|k'\rangle$  are the Fock states (eigenstates of  $\hat{H}_{\text{ph}}$  in Eq. 36). The light-matter Hamiltonian in Eq. 35 is in the form of  $\hat{H}$  in Eq. 8, where the quantum subsystem is  $\{|a\rangle, |b\rangle\} = \{|G, k\rangle, |m, k'\rangle\}$ . The exciton-photon-nuclear dynamics will be propagated using the PLDM approach (Eq. 13), and the cavity loss dynamics are accounted for by using the algorithm in Eq. 28. The polariton states of the molecule-cavity hybrid system are defined as

$$(\hat{H}_{\text{ex}} + \hat{H}_{\text{ph}} + \hat{H}_{\text{ex-ph}})|\Phi_\alpha\rangle = E_\alpha|\Phi_\alpha\rangle, \quad (42)$$

where the  $|\Phi_\alpha\rangle$  is the polariton state, with the polariton energy  $E_\alpha$ . Note that here we have not considered

any bath degrees of freedom ( $\hat{H}_{\text{R}}$  or  $\hat{H}_{\text{ex-R}}$ ) inside the definition of the polariton state and polariton energies, as opposed to the previous work that explicitly considers them inside the polariton definitions.<sup>48,49</sup>

The lifetime of the cavity mode is finite, due to the coupling between the cavity mode and the far-field photon modes outside the cavity. The detailed discussions for molecular cavity QED with cavity loss are provided in Appendix D of Ref. 47. Here, we use the following Lindblad jump operator<sup>47,50</sup> to model this process

$$\hat{L} = \hat{a} \otimes \hat{\mathcal{I}}_{\text{ex}} = \left[ \sum_{k=1}^{\infty} \sqrt{k} |k-1\rangle\langle k| \right] \otimes \hat{\mathcal{I}}_{\text{ex}}, \quad (43)$$

where  $|k\rangle$  is the vacuum's Fock state (eigenvector of Eq. 36), and  $\hat{\mathcal{I}}_{\text{ex}} = |G\rangle\langle G| + \sum_m |m\rangle\langle m| + \sum_{m \neq n} |m, n\rangle\langle m, n|$  is the identity operator for the electronic exciton subspace up to double excitation. The decay rate associated with  $\hat{L}$  is denoted as  $\Gamma$ . Note that the jump operator in Eq. 43, in principle, includes all possible transitions between Fock states  $|n+1\rangle$  and  $|n\rangle$ . In a practical simulation, one can choose to include the physically relevant decay channels. In the model calculation presented in this paper, we will only consider one decay channel (see Eq. 44). The system Lindblad jump operator in this subspace of Fock states can be written as

$$\hat{L} = |G, 0\rangle\langle G, 1| + \sqrt{2}|G, 1\rangle\langle G, 2| + \sum_m |m, 0\rangle\langle m, 1|. \quad (44)$$

The cavity loss rate from the Fock state  $|k=1\rangle$  to the Fock state  $|k=0\rangle$  is  $\Gamma$ , and the effective loss rate from the Fock state  $|k=2\rangle$  to the Fock state  $|k=1\rangle$  is  $2\Gamma$  due to  $\sqrt{k}$  in  $\hat{a}$  (see Eq. 43 and the second term in Eq. 44). For the  $\mathcal{L}$ -PLDM implementation (algorithm in Eq. 27-Eq. 28), we treat each of the term in Eq. 44 as the separate loss channel as  $\mathcal{L}_{\hat{L}}[\hat{\rho}] = \sum_\varphi \Gamma_\varphi (\hat{L}_\varphi \hat{\rho} \hat{L}_\varphi^\dagger - \frac{1}{2} \{ \hat{L}_\varphi^\dagger \hat{L}_\varphi, \hat{\rho} \})$ , where  $\hat{L}_\varphi \in \{|G, 0\rangle\langle G, 1|, |G, 1\rangle\langle G, 2|, |m, 0\rangle\langle m, 1|\}$ . For the  $|G, 0\rangle\langle G, 1|$  and each  $|m, 0\rangle\langle m, 1|$  channel, the loss rate is  $\Gamma$ . For the  $|G, 1\rangle\langle G, 2|$  channel, the loss rate is  $2\Gamma$ .

Even with the current simple model system, one can clearly understand the recently discovered polaron decoupling effect<sup>6,7,9</sup> when coupling the molecular system with the photonic DOF. For a monomer coupled to a single mode cavity, under the resonant condition,  $\bar{\epsilon} + \epsilon_m = \hbar\omega_c$ , the light-matter interaction term in Eq. 37 causes the light-matter hybridization between the  $|G\rangle \otimes |1\rangle$  with  $|m\rangle \otimes |0\rangle$ , resulting in the following polariton states

$$|\pm\rangle = \frac{1}{\sqrt{2}} [ |G\rangle \otimes |1\rangle \pm |m\rangle \otimes |0\rangle ]. \quad (45)$$

Note that since the exciton-phonon coupling is carried only through Eq. 33, and the phonon DOFs in Eq. 32 do not couple directly to the photonic DOFs in Eq. 36, the effective phononic coupling to the polariton state is

reduced. For example

$$\langle \pm | \hat{H}_{\text{ex-R}} | \pm \rangle = \pm \frac{1}{2} \sum_{\nu} c_{m,\nu} \hat{R}_{m,\nu}, \quad (46)$$

which is only half of the magnitude of  $\langle m | \hat{H}_{\text{ex-R}} | m \rangle = \sum_{\nu} c_{m,\nu} R_{m,\nu}$ . This effective reduction of the coupling for the phonon inside the cavity is referred to as the polaron decoupling effect.<sup>6,9</sup> A detailed discussion of the polaron decoupling effect under the collective coupling regime can be found in Ref. 7.

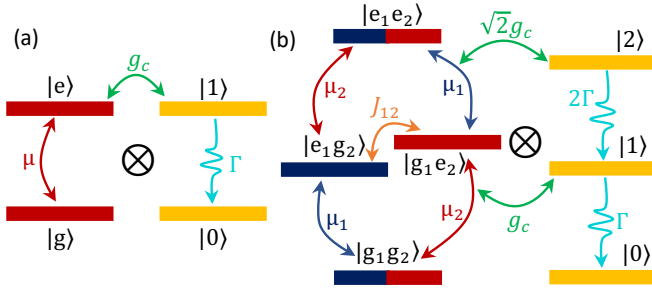


FIG. 1. Schematic illustration of the model system used in this work, with the energy level diagram for (a) the monomer coupled to the cavity and (b) the dimer coupled to the cavity.

Fig. 1 presents the schematic illustration of the model system considered in this work. Fig. 1(a) presents a model excitonic system coupled to cavity excitation, where the matter has onsite energy of  $\bar{\epsilon}$  and a transition dipole  $\mu$ . The matter couples to the cavity mode with coupling strength  $g_c$  (for monomer  $m = 1$ , and for the dimer, the coupling strength  $g_c(m)$  depends on the transition dipole magnitude  $\mu_m$ , see Eq. 39). The cavity mode has a loss rate of  $\Gamma$  for the decay of Fock states. Fig. 1(b) presents a molecular dimer coupled to a single cavity mode. Individual monomers in the dimer system have asymmetry in their energies ( $\epsilon_1 \neq \epsilon_2$ ) and their transition dipoles ( $\mu_1 \neq \mu_2$ ). Local excitons ( $|e_1, g_2\rangle$  and  $|g_1, e_2\rangle$ ) are coupled with strength  $J_{12}$ . In addition, the cavity has been tuned to the lower exciton. To complete the double excitation manifold required for the 2DES simulation, we also include the second excited Fock state,  $|g_1, g_2, 2\rangle$ . This state couples to  $|g_1, e_2, 1\rangle$  and  $|e_1, g_2, 1\rangle$  through Eq. 37 with strength  $\sqrt{2}g_c(m)$ . The cavity loss will cause the decay of  $|g_1, g_2, 2\rangle$  to  $|g_1, g_2, 1\rangle$  according to  $\hat{L}$  in Eq. 44, with a decay rate of  $2\Gamma$ .

#### IV. THE PLDM ALGORITHM FOR POLARITON 2DES SPECTRA

To simulate the 2DES spectra for the polaritonic system, we follow the previous procedure outlined in Ref. 19. Furthermore, we explicitly compute the contribution from individual Liouville pathways (Feynman diagrams) through Eq. 4a to Eq. 4d. The quantum DOFs, which are described as the exciton-Fock states

$\{|a\rangle, |b\rangle\} \equiv \{|G\rangle \otimes |k\rangle, |m\rangle \otimes |k'\rangle\}$  where  $|k\rangle$  and  $|k'\rangle$  are the Fock states (eigenstates of  $\hat{H}_{\text{Ph}}$  in Eq. 36). The nuclear DOFs are sampled from the initial Wigner distribution based on Eq. 10. The total initial condition for the molecule-cavity hybrid system (the system reduced density operator, see Eq. 15) is

$$\hat{\rho}_S(0) = \hat{\rho}^{(0)} \otimes \hat{\rho}_R = |G, 0\rangle\langle G, 0| \otimes \frac{1}{\mathcal{Q}} e^{-\beta \hat{H}_R}, \quad (47)$$

where  $\hat{\rho}^{(0)}$  is the initial state for the exciton-photonic subsystem (the quantum subsystem), and  $\hat{\rho}_R$  is the thermal initial condition for the phonon,  $\mathcal{Q} = \text{Tr}_R[e^{-\beta \hat{H}_R}]$  is the phonon bath partition function, and  $\beta = 1/k_B T$  with  $T$  as the temperature and  $k_B$  as the Boltzmann factor.

For each of these initial conditions, we generate a trajectory by following the steps below,

1. For  $\hat{\rho}^{(0)} = |G, 0\rangle\langle G, 0|$ , apply the first dipole operator  $\hat{\mu}$  (Eq. 40) to obtain  $\tilde{\rho}^{(1)} \equiv \hat{\mu}(t_0)\hat{\rho}^{(0)}$ . For example, if  $\hat{\mu}(t_0) = \mu_m(|G\rangle\langle m| + |m\rangle\langle G|)$ , then  $\tilde{\rho}^{(1)} = \mu_m|m, 0\rangle\langle G, 0|$ . Use the focused initial condition<sup>19,46</sup> to assign initial values of the mapping variables according to the matrix of  $\tilde{\rho}^{(1)} \equiv \hat{\mu}(t_0)\hat{\rho}^{(0)}$ . For example, if  $\tilde{\rho}^{(1)} = |a\rangle\langle b|$ , then

$$x_a^F = 1, \quad p_a^F = 1, \quad x_b^B = 1, \quad p_b^B = -1. \quad (48)$$

and all other mapping variables are set to zero. If  $\tilde{\rho}^{(1)} = \sum_{a,b} r_{ab}|a\rangle\langle b|$  (which is always real), then one applies the focused initial condition for each pair of  $\{a, b\}$  and weight the contribution with  $r_{ab}$ .

2. For each non-zero element in  $\tilde{\rho}^{(1)}$ , perform the  $\mathcal{L}$ -PLDM dynamics propagation using Eq. 29 for a duration of  $t_1$ .
3. At  $t = t_1$ , according to each Liouville pathway  $R_1^{(3)}(t_1, t_2, t_3)$  (Eq. 4a) to  $R_4^{(3)}(t_1, t_2, t_3)$  (Eq. 4d), apply the second dipole operator  $\hat{\mu}(t_1)$  on  $\tilde{\rho}^{(1)}(t_1)$  to get  $\tilde{\rho}^{(2)}(t_2)$  (note for  $R_1^{(3)}$  and  $R_3^{(3)}$ ,  $\hat{\mu}(t_1)$  act from the right-hand side, and for  $R_2^{(3)}$  and  $R_4^{(3)}$ ,  $\hat{\mu}(t_1)$  act from the left-hand side). The other four Liouville pathways are just the complex conjugate (c.c.) of Eq. 4a-Eq. 4d and can be simply obtained by taking c.c. of the  $\mathcal{L}$ -PLDM results of Eq. 4a-Eq. 4d.
4. Perform Monte-Carlo importance sampling as described in Ref. 19 to evaluate  $\tilde{\rho}^{(2)}(t_2)$ , with the following procedure

- (a) Expand  $\tilde{\rho}^{(2)}(t_2)$  as

$$\tilde{\rho}^{(2)} = \sum_{ab} r_{ab} e^{i\theta_{ab}} |a\rangle\langle b|. \quad (49)$$

- (b) Generate the cumulative distribution function (CDF),

$$d_{ab} = \frac{r_{ab}}{\sum_{ij} r_{ij}}. \quad (50)$$

- (c) Sample a uniform random number,  $\zeta \in [0, 1]$ .  
 (d) Find the index,  $K \equiv ab$ , for which,

$$d_{K-1} < \zeta \leq d_K, \quad (51)$$

where  $K - 1$  is the previous index of  $K$  when generating the CDF. (For example, for a 3-level system, the CDF will be made of  $[d_{00}, d_{01}, \dots, d_{22}]$ . If  $K \equiv 02$ , the relation (Eq. 51) will be  $d_{01} < \zeta \leq d_{02}$ .)

- (e) With  $K = ab$ , set

$$\tilde{\rho}^{(2)} = |a\rangle\langle b|, \quad (52)$$

and use the focused initial condition to sample the mapping variables (as described in step 3). The nuclear DOFs remains the same at this step.

- (f) The trajectory is weighted by the phase  $e^{i\theta_{ab}}$  after the time  $t_2$ .

5. For each  $t_2$ , repeat the steps 3 and 4 for  $t_3$  time units to get  $\tilde{\rho}^{(3)}(t_3)$ .

6. At  $t_3$ , apply the final dipole operator and multiply all the previous three weights. The final third-order response is obtained by taking a trace and multiplying by  $-i$ .

These steps are calculated for each of the Liouville pathways (Eq. 4a to Eq. 4d). To demonstrate the details of the procedure, we present a concrete example of the evolution of the density matrix for  $R_1^{(3)}$  (Eq. 4a) in Fig. 2. The estimator for  $R_1^{(3)}$  after step (6) is expressed as

$$R_1^{(3)}(t_3, t_2, t_1) = (-i)^3 \text{Tr}_{\text{ex}} \text{Tr}_{\text{ph}} [\hat{\mu}_3 \tilde{\rho}^{(3)}(t_3)], \quad (53)$$

where  $\text{Tr}_{\text{ex}}$  and  $\text{Tr}_{\text{ph}}$  represent the trace over the excitonic and photonic DOFs, separately. The above procedure can either be terminated after acting  $\hat{\mu}(t_2)$  to get the 1<sup>st</sup> order non-linear spectra (e.g. transient absorption spectra) or can also be continued with further perturbations to get the  $n$ <sup>th</sup> order spectra. The advantage of the PLDM algorithm is its scalability, where (1) each trajectory can be propagated independently, and (2) for each trajectory, any particular branch ( $t_1, t_2, t_3$ ) can be propagated independently of any other branch ( $t_1', t_2', t_3'$ ). Thus, the algorithm is highly parallelizable, and the scaling of the non-linear spectroscopy computation can be efficiently controlled in high-performance computing facilities.

## V. COMPUTATIONAL DETAILS

### A. Model parameters

For the monomer (Fig. 1a), we used  $\bar{\epsilon} = 10,000 \text{ cm}^{-1}$  (which is 1.24 eV). The monomeric site

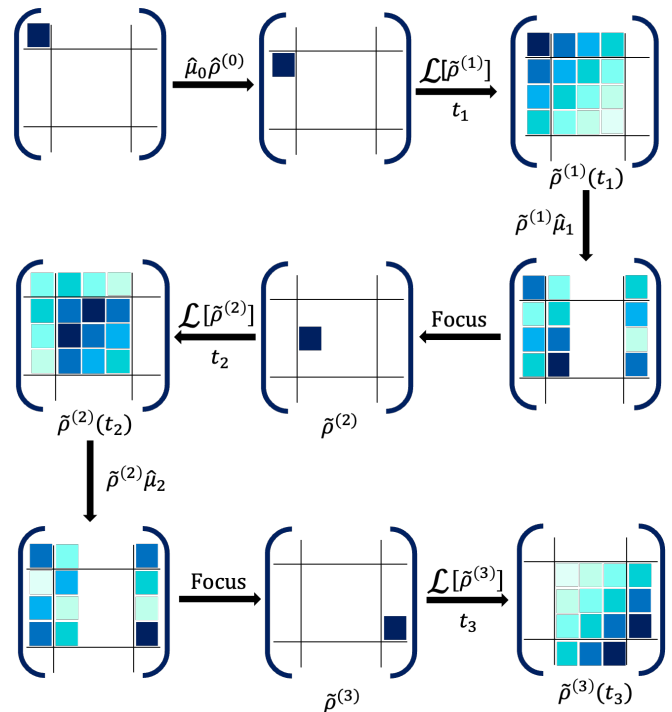


FIG. 2. Schematic illustration of the 2DES simulation algorithm, with one possible path (see Eq. 4 for all possible paths). The color gradients imply the magnitude of the density matrix elements.  $\mathcal{L}$  indicates the overall time evolution by the  $\mathcal{L}$ -PLDM approach (see Eq. 29), and  $\mu_i \tilde{\rho}^{(i)}$  (or  $\tilde{\rho}^{(i)} \mu_i$ ) indicate the dipole operator acting on the density matrix from the left-hand (right hand) side at time  $t = t_i$ .

coupled to a phonon bath, discretized by  $N_\nu = 100$  independent bath modes, with index  $\nu \in [1, 100]$ , has parameters sampled from Eq. 34 using the procedure outlined in Ref. 46 (or more generally, Ref. 51)

$$c_\nu = 2\sqrt{\lambda \frac{\tan^{-1}(\omega_{\max} \tau_c)}{\pi N_\nu \omega_\nu}}, \quad (54a)$$

$$\omega_\nu = \frac{1}{\tau_c} \tan\left(\frac{\nu}{N_\nu} \tan^{-1}(\omega_{\max} \tau_c)\right), \quad (54b)$$

where  $\omega_{\max} \gg \omega_0$  is the maximum frequency while discretizing the bath frequencies. Here, we choose  $\omega_{\max} = 5 \omega_0$ . The bath parameters are  $\omega_0 = \tau_c^{-1} = 18 \text{ cm}^{-1}$  (which is 2.2 meV) and  $\lambda = 50 \text{ cm}^{-1}$  (which is 6.2 meV). The characteristic phonon frequency  $\omega_0$  leads to a bath correlation function decay timescale of  $\tau_c = 300 \text{ fs}$ . The cavity coupling strength,  $g_c$ , is varied from  $50 \text{ cm}^{-1}$  (which is 6.2 meV) to  $1000 \text{ cm}^{-1}$  (which is 124 meV) for linear spectra (Fig. 3). For 2DES in Fig. 5,  $g_c$  is varied between  $100 \text{ cm}^{-1}$  (12 meV) and  $500 \text{ cm}^{-1}$  (62 meV). The cavity loss rate  $\Gamma$  is varied between 0 meV and 500 meV for linear spectra (Fig. 3) and between 0 meV and 20 meV (which is  $161 \text{ cm}^{-1}$ ) for 2DES in Fig. 5. The cavity quality factor is defined as  $Q = \omega_c / \Gamma$ . For the resonant case,  $\omega_c = \bar{\epsilon}$ , and  $Q = 62$



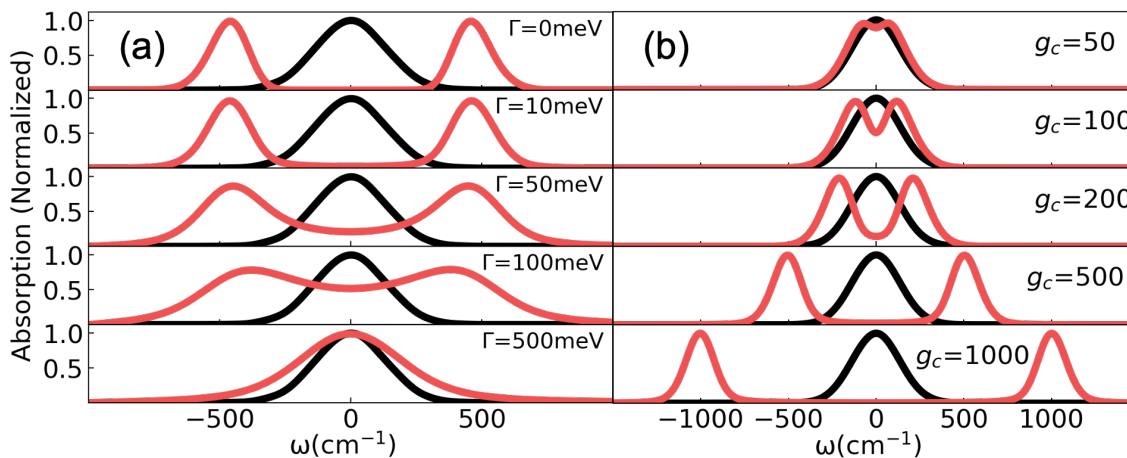


FIG. 3. Linear absorption spectra of a monomer outside the cavity (black) and inside the cavity (red), with (a) varying the cavity loss rates  $\Gamma$  and a fixed light-matter coupling strength  $g_c \approx 456 \text{ cm}^{-1}$ , and (b) varying cavity coupling strength  $\hbar g_c$  and a fixed cavity loss rate of  $\Gamma = 10 \text{ meV}$ .

for  $\Gamma = 20 \text{ meV}$ .

For the dimer (Fig. 6 and Fig. 7), we used the mean onsite energy  $\bar{\epsilon} = 10,000 \text{ cm}^{-1}$  (1.24 eV) and  $\epsilon_1 - \epsilon_2 = 100 \text{ cm}^{-1}$ . The ratio of dipoles for individual monomeric sites is taken to be  $\mu_1/\mu_2 = -5$ , and so is the light-matter coupling constant  $g_c(1)/g_c(2) = -5$ . We use 100 discretized bath modes for each site from Eq. 34 with  $\omega_0 = 200 \text{ cm}^{-1}$  (which is 24.8 meV) and  $\lambda = 200 \text{ cm}^{-1}$ . The characteristic phonon frequency  $\omega_0$  gives a bath correlation decay timescale of  $\tau_c = 50 \text{ fs}$ . The coupling strength,  $g_c$ , is varied between  $100 \text{ cm}^{-1}$  (which is 12 meV) and  $500 \text{ cm}^{-1}$  (which is 62 meV) for Fig. 6. In Fig. 7,  $g_c = 500 \text{ cm}^{-1}$  and  $\Gamma = 10 \text{ meV}$  is used.

The initial nuclear condition  $\hat{\rho}_R$  (see Eq. 47) is described by its Wigner transform for the PLDM approach, with the following analytic expression

$$[\hat{\rho}_R]_W(R_0, P_1) = \prod_{\nu} 2 \tanh\left(\frac{\beta \hbar \omega_{\nu}}{2}\right) \exp\left[-\tanh\left(\frac{\beta \hbar \omega_{\nu}}{2}\right) \left(\frac{\omega_{\nu}^2 R_0^2}{\hbar^2} + \frac{P_1^2}{\hbar^2 \omega_{\nu}^2}\right)\right]. \quad (55)$$

The initial nuclear configurations  $(R_0, P_1)$  are sampled from the Gaussian random distribution, with width according to Eq. 55.

## B. Simulation Details

All the simulations are performed under room temperature  $T = 300 \text{ K}$ . For the monomer, the linear spectra in Fig. 3 were computed using Eq. 2, which is a smoothed Fourier transform of the response function  $R^{(1)}(t)$  in Eq. 1. We obtain  $R^{(1)}(t)$  (Eq. 1) by performing the  $\mathcal{L}$ -PLDM simulation using  $10^5$  trajectories, with the dynamics governed in Eq. 29. The initial nuclear configurations are sampled from Eq. 10, and the initial mapping

variables are chosen based on the focused initial condition (see Eq. 48). The total simulation time is 300 fs for the  $R^{(1)}(t)$ , which guarantees a converged  $R^{(1)}(\omega)$ .

The 2DES spectra in Fig. 5, Fig. 6, and Fig. 6 are calculated with  $10^4$  trajectories, although convergence begins to appear with only  $10^3$  trajectories. The color bar corresponds to 2DES signal intensities normalized with respect to the maximum peak intensity for the 2DES at  $t_2 = 0 \text{ fs}$  for each simulation. The monomer 2DES calculation involves  $T_1 = T_3 = 300 \text{ fs}$  with a nuclear time step of 1 fs and 120 electronic time steps for each nuclear time step. For the 2DES intensity plot in Fig. 8 we used  $10^3$  trajectories. This calculation involved  $T_1 = T_3 = 50 \text{ fs}$  with a nuclear time step of 0.5 fs and 60 electronic steps per nuclear time step. In Fig. 8, all peak intensities are calculated by selecting a small region  $\Delta\omega = \pm 10 \text{ cm}^{-1}$  around the off-diagonal peak location and integrating the intensity of the region, then normalized with respect to the integrated value at  $t_2 = 0 \text{ fs}$ .

## VI. RESULTS AND DISCUSSION

We present the computed linear absorption and purely absorptive-2DES of a monomer and an asymmetric dimer coupled to a single-mode cavity. We investigate the effect of light-matter coupling and cavity loss on the photophysical properties of exciton-polaritons.

### A. Linear spectra

Fig. 3 presents the linear absorption spectra of a monomer coupled to the cavity by either varying cavity loss rate,  $\Gamma$  (Fig. 3a), or by varying the light-matter coupling strength,  $g_c$  (Fig. 3b). The black curve in all panels represents the bare monomer molecular absorption spec-

tra, with the broadening coming from couplings to collective bath-mode fluctuations. The red curves represent the spectra of a monomer coupled to a cavity mode.

In Fig. 3a, we fix the light-matter coupling  $g_c = 57$  meV ( $\approx 456$  cm<sup>-1</sup>), while varying the cavity loss  $\Gamma$ . For  $\Gamma = 0$  meV (top panel), we observe a Rabi splitting of the monomer peak into upper and lower polaritons. The two polariton peaks (red curves) have a reduced line width compared to that of the bare monomer, hinting at the effective decoupling of polariton states from the phonon bath,<sup>6,9</sup> due to the fact that the photonic DOF is not directly coupled to the phonon (nuclear bath), see Eq. 46. Further, as we continue to increase the cavity loss, we see essentially the same splitting, but with extra broadening relative to the no-loss cavity case. This is expected as the cavity loss rate adds another relaxation channel, *i.e.*, the loss can also be thought of as an additional set of bath modes now attached to the upper and lower polariton states. At a very high loss rate ( $\Gamma \gg g_c$ ), we start to see that two polariton peaks begin to merge into one, indicating that the strong-coupling condition is no longer fulfilled.

Fig. 3b presents the linear spectra for a fixed cavity loss rate  $\Gamma = 10$  meV, with an increase in coupling strength  $g_c$ . The Rabi splitting of upper and lower polaritons increases. When  $g_c = 50$  cm<sup>-1</sup> or  $100$  cm<sup>-1</sup>, the strong coupling condition that  $g_c \gg \Gamma, \kappa$  is not fulfilled and there is no apparent Rabi splitting. As the  $g_c$  increases, the Rabi splitting appears. The broadening of individual polariton peaks is the same in all the above cases, which is expected from the fixed cavity loss rate (which is equivalent to fixing the photon loss bath parameters that couples to the cavity mode  $q_c$ , and hence the same distribution of frequencies).

We note that in Fig. 3a, there is a slight contraction of the Rabi splitting when we increase the cavity loss  $\Gamma$ , for example, when we increase  $\Gamma$  from 50 meV to 100 meV. This contraction is caused by cavity loss. When explicitly considering the cavity loss rate  $\Gamma$  and the matter loss rate  $\kappa$ , the Jaynes-Cummings model Hamiltonian in the  $\{|G, 1\rangle, |e, 0\rangle\}$  subspace is expressed as<sup>52-54</sup> (without including the field zero-point energy  $\hbar\omega_c/2$ )

$$\hat{\mathcal{H}}_{\text{JC}} = \begin{bmatrix} E_G + \hbar\omega_c - i\frac{\kappa}{2} & \hbar g_c \\ \hbar g_c & E_e - i\frac{\Gamma}{2} \end{bmatrix}. \quad (56)$$

Under the resonant condition that  $E_G + \hbar\omega_c = E_e$ , and directly diagonalizing the above Hamiltonian, one obtains the following complex eigenvalues<sup>52,53</sup>

$$E_{\pm} = E_e - i\frac{\kappa + \Gamma}{4} \pm \sqrt{\hbar^2 g_c^2 - \left(\frac{\kappa - \Gamma}{4}\right)^2}, \quad (57)$$

with the real part corresponding to the eigenenergy and the imaginary part corresponding to the loss/broadening. For the model system investigated here,  $\kappa = 175$  cm<sup>-1</sup> (from directly fitting the numerical value of  $R^{(1)}(\omega)$ , the black curve in Fig. 3 to a gaussian), and for  $\Gamma = 100$  meV (806 cm<sup>-1</sup>), the Rabi splitting is reduced (see Eq. 57),

causing the peak of the upper and lower polariton to shift from  $\pm 456$  cm<sup>-1</sup> to  $\pm 428$  cm<sup>-1</sup>, which is in semi-quantitative agreement with our numerical results. In fact, the agreement between the analytic answer from Eq. 57 and the simulated spectra are incredibly good, across all cavity loss  $\Gamma$  we explored.

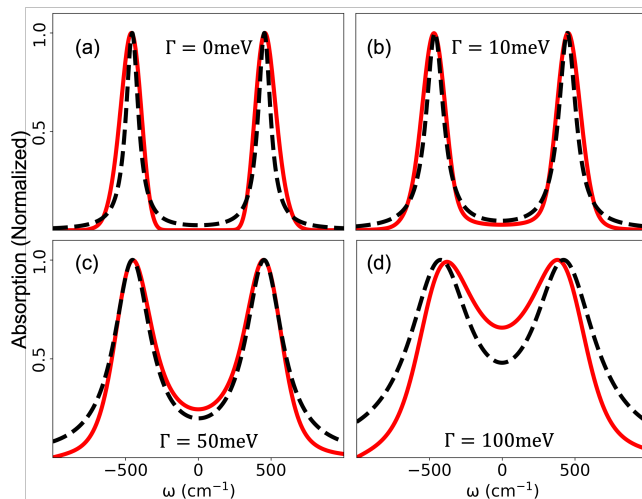


FIG. 4. A comparison between the  $\mathcal{L}$ -PLDM simulated linear spectra (red solid lines) with the analytic expression in Eq. 58 (black dotted lines), for the same model system presented in Fig. 3. The coupling strength  $g_c \approx 456$  cm<sup>-1</sup> is fixed, whereas the cavity loss rate  $\Gamma$  varies. The analytic curve in Eq. 58 is obtained with peaks from the real part of Eq. 57 and Lorentzian broadening of the width given by the imaginary part of Eq. 57.

In Fig. 4, we present a direct comparison between the simulated linear spectra (red) with the polariton absorption modeled by the analytic expression (black dashed) composed of adding two Lorentzian lineshapes for the  $|+\rangle$  and  $|-\rangle$  polaritons as follows

$$R^{(1)}(\omega) \propto \sum_{\alpha=\pm} |\mu_{\alpha G}|^2 \cdot \frac{1}{\pi} \cdot \frac{\sigma_{\alpha}}{(\hbar\omega - \hbar\omega_{\alpha})^2 + \sigma_{\alpha}^2}, \quad (58)$$

with the polariton frequency  $\omega_{\alpha} = (\Re[E_{\alpha}] - E_G)/\hbar$  taken from the real part of Eq. 57, and the width  $\sigma_{\alpha} = \Im[E_{\alpha}] = (\kappa + \Gamma)/4$  taken from the imaginary part of Eq. 57. For a large cavity loss rate  $\Gamma$ , the term inside the square root becomes negative so that the real solution no longer exists and the two polariton peaks merge into one. Also, the width of the polariton peak, based on Eq. 57, is  $(\kappa + \Gamma)/4$ . As the cavity loss rate  $\Gamma$  increases, the width of the polariton peak will also increase. Under the  $\Gamma = 0$  limit, the polariton peak has a width of  $\kappa/4$ , two times smaller than the original exciton width  $\kappa/2$ , indicating the polaron decoupling effect from the light-matter interaction<sup>7,9</sup> (see Eq. 46 and discussions).

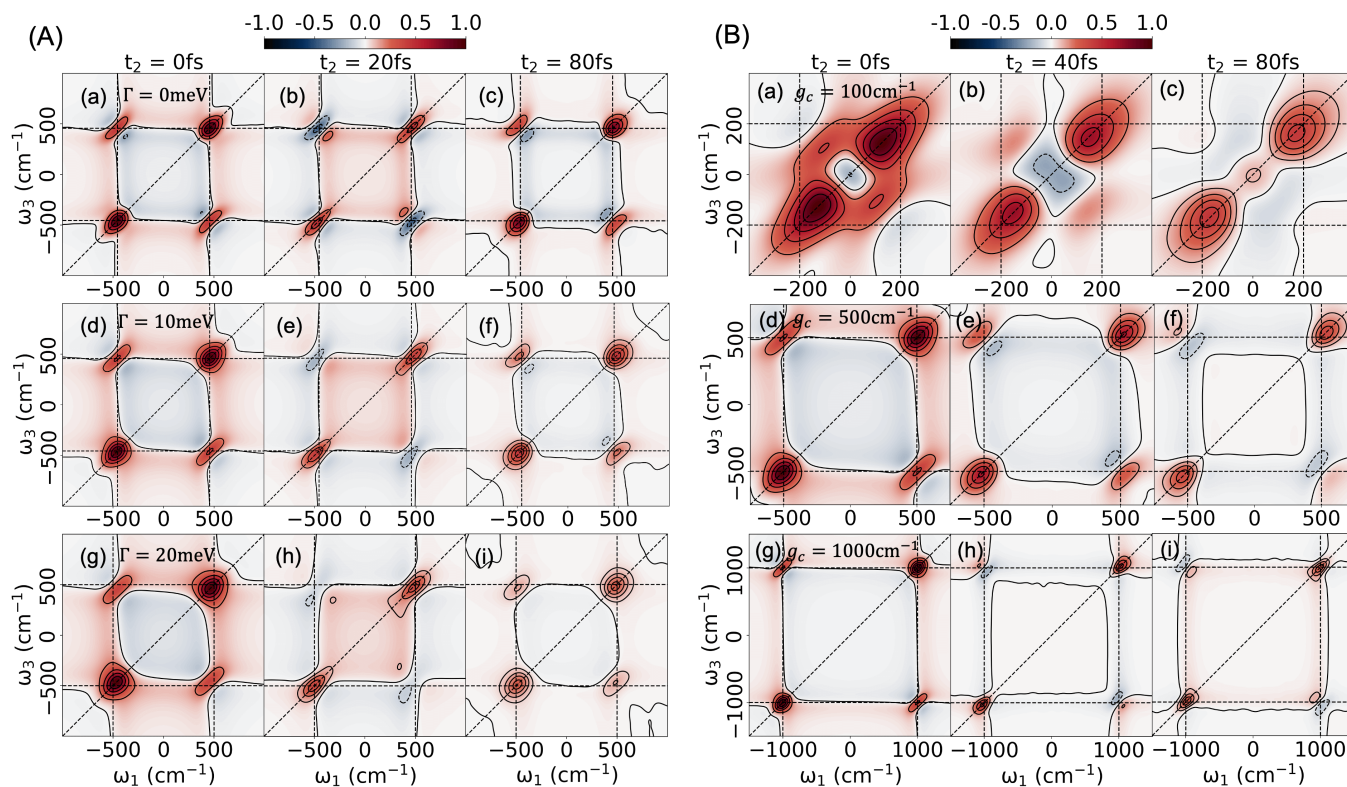


FIG. 5. Purely absorptive polaritonic 2DES for a monomer coupled to the cavity. (A) The molecule-cavity hybrid system is kept under a fixed light-matter coupling strength  $\hbar g_c = 57$  meV with various cavity loss rates, with (a)-(c)  $\Gamma = 0$  meV, (d)-(f)  $\Gamma = 10$  meV and (g)-(i)  $\Gamma = 20$  meV. The 2DES spectra are presented at different waiting times  $t_2$  for  $t_2 = 0$  fs (left column),  $t_2 = 20$  fs (middle), and  $t_2 = 80$  fs (right column). (B) The hybrid system is kept under a fixed cavity loss of  $\Gamma = 10$  meV, and with various light-matter coupling strengths of (a)-(c)  $\hbar g_c = 0$  meV, (d)-(f)  $\hbar g_c = 10$  meV and (g)-(i)  $\hbar g_c = 20$  meV.

## B. Purely absorptive 2D polariton spectra of monomer in cavity

Fig. 5 presents the purely absorptive 2DES polariton spectra (see Sec. IV) of a monomer coupled to a single-mode cavity. Fig. 5A represents the polariton 2DES spectra with various cavity loss rates  $\Gamma$  and with a fixed coupling strength of  $g_c = 57$  meV. Fig. 5B presents the polariton 2DES spectra with various coupling strengths  $g_c$  at a fixed cavity loss rate of  $\Gamma = 10$  meV. For all 2DES plots, the horizontal and vertical dotted lines indicate the polariton peak locations  $\pm g_c$  along the emission and excitation axes. Note that the actual peak position will be shifted with different cavity loss rates, as indicated by Eq. 57 and Fig. 3.

In Fig. 5A, panels (a)-(c) provides the 2D spectra of monomers coupled to a cavity with no cavity loss. We observe the Rabi splitting of the lower and upper polariton diagonal peaks at  $t_2 = 0$  fs. These peaks are also stretched along the diagonal, indicating the inhomogeneous distribution caused by the low-frequency bath modes (see Eq. 32) coupled to the exciton (Eq. 33), and also both upper and lower polaritons (Eq. 46). The characteristic off-diagonal coherence peaks in the 2D spectra are direct indications of the coupling between the

exciton and the cavity, described in Eq. 37. With an increase in waiting time  $t_2$ , the off-diagonal coherence peaks oscillate and the diagonals slowly become more homogeneously broadened (along the anti-diagonal direction) due to spectral diffusion, which arises mainly due to the decay of bath correlation and the loss of the initial memory of the system (commonly referred to as the circularisation), making the excitation axis  $\omega_1$  more independent of the emission axis  $\omega_3$ .

With an increase in cavity loss to  $\Gamma = 10$  meV in panels (d)-(f) or to  $\Gamma = 20$  meV in panels (g)-(i), one observes two prominent features in the 2D spectra. (1) Both the diagonal and the off-diagonal peaks become more homogeneous (further broadened along the anti-diagonal direction), even at  $t_2 = 0$  fs. This is purely due to the effect of the Lindblad treatment for the cavity loss, which adds a homogeneous dephasing channel for the decay of the coherences in the reduced system density matrix, thus homogenizing the peaks. The homogeneous nature of the photonic bath is a direct result of Markovian treatment via Lindbladian, which is equivalent to a bath described by a very high cutoff frequency. (2) The second laser pulse puts most of the ensemble in the population state (see Fig. S2 in the Supplemental Materials), and so a decay in signal intensity along  $t_2$  can be mostly attributed

to excited population decay. Now, the addition of an extra loss channel from the cavity causes the populations to decay proportional to  $e^{-\Gamma dt}$  (Lindblad-type decay). Therefore, with an increase in the cavity loss rate  $\Gamma$ , one observes a faster decay of the signal intensity at a given  $t_2$ . This is obvious when comparing panel (e) for  $\Gamma = 10$  meV or panel (h) for  $\Gamma = 20$  meV to panel (b) for  $\Gamma = 0$ .

Fig. 5B presents the polariton 2DES spectra when varying the light-matter coupling strength  $g_c$  at a fixed cavity loss rate  $\Gamma = 10$  meV. With an increase in  $g_c$ , the separation between the lower and upper polariton peaks increases, just like those in the linear spectra as presented in Fig. 3b. As a result of Rabi splitting, the overlap between the diagonal and cross peaks decreases, making it easier to track the behavior of individual peaks.

### C. Enhancing Polariton Coherence through Polaron Decoupling

In Fig. 6, we present the purely absorptive 2D polariton spectra (Eq. 7) of a coupled dimer inside a lossless cavity for various coupling strengths  $g_c$ , from  $g_c = 100 \text{ cm}^{-1}$  for panels (a)-(c), to  $g_c = 200 \text{ cm}^{-1}$  for panels (d)-(f), and to  $g_c = 500 \text{ cm}^{-1}$  for panels (g)-(i). The cavity loss rate is set to be  $\Gamma = 0$  for clarity. The detailed model parameters for the phonon bath are provided in Sec. V A. In short, a very fast phonon bath relaxation time  $\tau_c = 50$  fs combined with large reorganization energy  $\lambda = 200 \text{ cm}^{-1}$  causes the bath correlation function to decay before the bath coordinates relax to the excited-state minima. This causes the system to dephase very quickly, as can also be confirmed by the coherence dynamics of the reduced density matrix (and confirmed with Fig. 8a-b). Further, the bath parameter regime ( $\omega_0 = 200 \text{ cm}^{-1}$ ) causes homogeneous broadening of the individual polariton peaks. The large reorganization of the phonon bath also causes a large spread of 2D lineshapes and a large shift of polariton peaks from the eigenvalue in Eq. 57. For  $g_c = 500 \text{ cm}^{-1}$  and  $\Gamma = 10$  meV, the  $t_2 = 0$  fs 2DES result is provided in the panel (l) of Fig. 7, which is similar to Fig. 6g, except with a lower intensity for the signal. Additional 2DES results for various  $\Gamma$  and  $t_2$  are provided in Fig. S5 of the Supporting Information.

In Fig. 7, we present the signal decomposition of for the case of  $g_c = 500 \text{ cm}^{-1}$  and  $\Gamma = 10$  meV with the aim of providing an intuitive understanding of the origin of different peaks in Fig. 6. These pathways can be classified as ground state bleaching (GSB), stimulated emission (SE), and excited state absorption (ES), each with rephasing and non-rephasing contributions. The contribution for each term is provided in Eq. 5 and the discussion below. The Feynman diagrams for these Liouville pathways are provided in Fig. S2 of the Supporting Information. In Fig. 7, we only present the signal from GSB (panels a-c) and SE (panels d-f). The excited state absorption (ES) signals are much weaker compared to GSB and SE, and do not make a significant contribution to the totally ab-

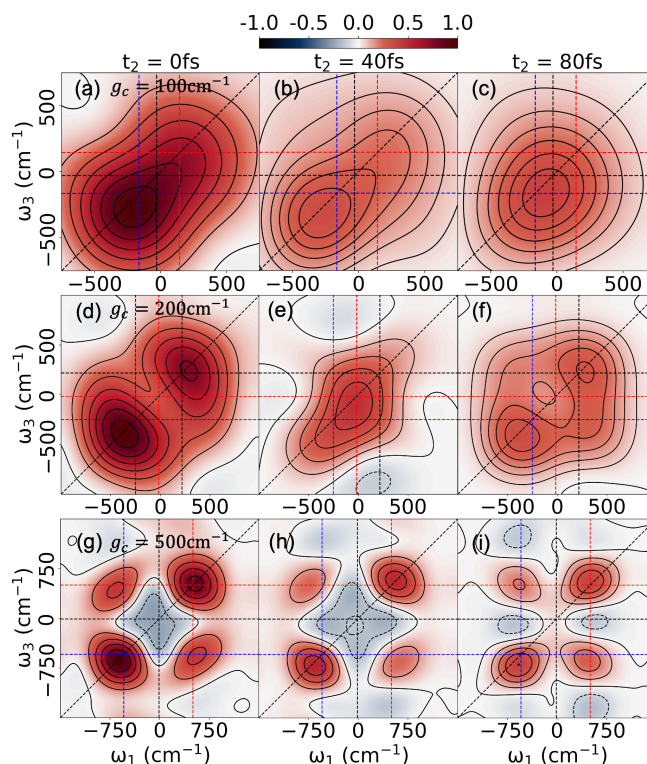


FIG. 6. Purely absorptive 2DES of the exciton dimer coupled to the cavity, with (a)-(c)  $g_c = 100 \text{ cm}^{-1}$ , (d)-(f)  $g_c = 200 \text{ cm}^{-1}$ , (g)-(i)  $g_c = 500 \text{ cm}^{-1}$  for a lossless cavity ( $\Gamma = 0 \text{ meV}$ ).

sorptive signal. The ES results are provided in Fig. S4 of the Supporting Information.

Decomposing the purely absorptive signal into individual contributions allows us to estimate the contributions of individual energy transfer processes in the molecule-cavity hybrid system. Because we have two exciton states for the system, hybridizing with the photonic excitation results in three polariton states, which we denote as  $|+\rangle$  (upper polariton),  $|D\rangle$  (middle polariton), and  $|-\rangle$  (lower polariton) states. The detailed expressions of these three polaritons are provided Sec. I of the Supporting Information, where the middle polariton state has a relatively small contribution of the photonic excitation, hence is denoted as the “dark” state  $|D\rangle$ . The molecular transition dipoles between  $|G\rangle$  and these polariton states are also provided in the Supporting Information, Sec. I.

For the GSB (panels a-c) and SE pathways (d-f), we only observe peaks at upper and lower polariton frequencies and also at the coherence position between upper and lower polaritons. This can be directly understood by looking at the dipole matrix elements of this particular system (see Supporting Information, Sec. I), where there are large transition dipoles from the ground state to  $|\pm\rangle$  polaritons. The middle polariton (dark state  $|D\rangle$ ) is not visible in the 2D signal, because the transition dipole from the ground state to the middle polariton is very small. In fact,  $\mu_{GD} = \langle D|\hat{\mu}|G\rangle$  is  $\approx 35$  times smaller

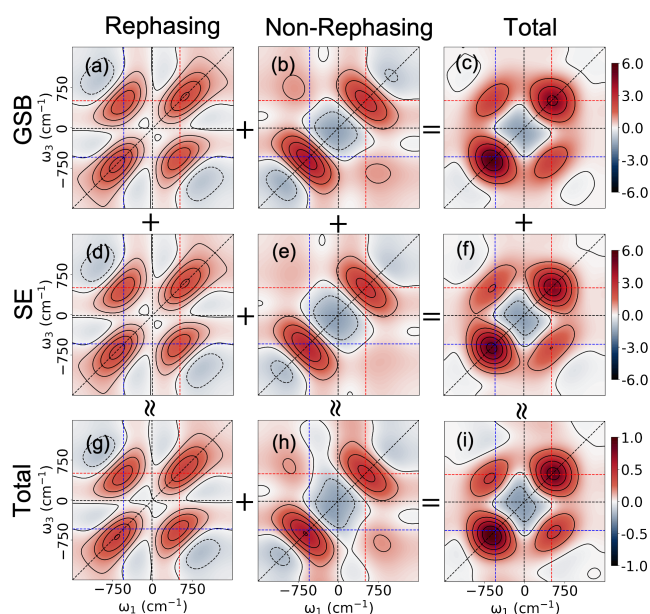


FIG. 7. Signal decomposition of the purely absorptive 2DES spectra of the exciton dimer coupled to the cavity, with the cavity loss rate  $\Gamma = 10\text{meV}$  and the light-matter coupling strength  $\hbar g_c = 500\text{cm}^{-1}$ . The signal is decomposed into the GSB (a-c) and SE (d-f) contribution with their rephasing (a, d, g) and non rephasing (b, e, f) components for  $t_2 = 0$  fs. The excited state absorption signal (see Fig. S4 of the Supplemental Materials) is much weaker compared to the GSB and SE components.

than the corresponding transition dipoles to the upper polariton  $\mu_{+G}$  or the lower polariton  $\mu_{-G}$ . Since the GSB and SE pathways are only involved in transitions between the ground and first excitation manifold, we do not observe the signatures of the dark state due to its very low transition amplitude ( $|\mu_{GD}|^2 \propto (1/35)^2 = 0.0008$ ). In Fig. S3 of the Supporting Information, we further present the contribution of different polariton states to the GSB and SE peaks, based on the magnitude of  $|\mu_{\alpha G}|^2$  (where  $|\alpha\rangle \in \{|+\rangle, |D\rangle, |-\rangle\}$ ). The full results of  $t_2 > 0$  spectra are presented in Fig. S5 of the Supporting Information. With a finite cavity loss ( $\Gamma = 10$  meV), one can expect a similar trend as shown in Fig. 5A. The 2DES peaks will be more homogeneously broadened and the peak intensity will be lost at a faster rate, with an increased loss rate, as shown in Fig. S5 of the Supporting Information.

Fig. 8a and Fig. 8b present intensities of the lower diagonal and upper cross-peaks as a function of  $t_2$ , with  $\Gamma = 0$  meV, and various light-matter coupling strengths  $g_c$ . The orange curve corresponds to the 2DES peak intensities of a molecular system outside the cavity (or  $g_c = 0$ ). As we can see, there is no apparent coherent oscillation in the system due to the large reorganization of the phonon bath that causes fast decoherence. When coupling to the cavity, we see that with an increase in the light-matter coupling, the coherence oscillations become more prominent and last for more than 200 fs at room

temperature. This is caused by the polaron decoupling mechanism,<sup>7,9</sup> as explained by Eq. 46. This is because by coupling to the photonic DOFs, the effective coupling between the polariton state and the phonon (nuclei) is reduced.<sup>6,7,9</sup> Therefore, coupling molecules to an optical cavity can provide a way to prolong the coherence of the hybrid system compared to the bare molecules. Similar enhanced electronic coherence has been experimentally observed by collectively coupling organic molecules with the optical cavity.<sup>9</sup> Again, the characteristic phonon frequency  $\omega_0 = 200\text{cm}^{-1}$  used in this model is much smaller than the Rabi splitting created in this case, so the oscillation observed in Fig. 8b is less likely due to the vibrational coherence as often observed in natural light-harvesting systems.<sup>55–57</sup>

Fig. 8c and Fig. 8d present the intensities of the lower diagonal and upper cross peaks, respectively, as a function of  $t_2$  with the light-matter coupling strength of  $\hbar g_c = 500\text{cm}^{-1}$  (62 meV) for various cavity loss rates. As can be suspected, adding cavity loss causes an equivalent effect to adding a dissipative bath for the cavity mode. Thus, with an increased cavity loss, one observes an increase in the decoherence among polariton states. It should be noted that even for an experimentally accessible cavity loss rate of  $\Gamma = 10$  meV and Rabi splitting  $\Omega_R = 2\hbar c \approx 124$  meV we still observe a long-lived polaritonic coherence (for  $t > 200$  fs) at room temperature, much longer than the typical electronic decoherence of the molecule (see the orange curve in Fig. 8) whose exciton-phonon re-organization energy is  $\lambda = 24.8$  meV ( $200\text{cm}^{-1}$ ). Similar experimental conditions for the  $\lambda$ ,  $\Gamma$  and  $\Omega_R$  have been recently achieved when coupling CdSe nanoplatelets to a dielectric optical cavity.<sup>48</sup>

## VII. CONCLUSION

We developed a new theoretical approach to simulate polariton linear and non-linear spectra, which fully account for the non-Markovian exciton-phonon couplings and the effect of cavity loss. This approach is based on combining the partial linearized density matrix (PLDM) approach,<sup>19–22</sup> which is a non-adiabatic path-integral formalism, and a new Lindblad method that exactly maps the Lindblad dynamics with a stochastic evolution of the mapping variables. We refer to this approach as the  $\mathcal{L}$ -PLDM method. Using this approach, we simulated the linear and third-order response functions, and upon Fourier transform, obtain the corresponding optical spectra.

Using the Jaynes-Cummings (JC) type model Hamiltonian, we further investigated the optical spectra influenced by the light-matter coupling strength  $\hbar g_c$  and the cavity loss rate  $\Gamma$ . In this work, we focused on two particular model systems, an exciton monomer coupled to a single-mode cavity, and an exciton dimer coupled to a single-mode cavity. For an exciton monomer coupled to the cavity, the linear spectra obtained from the  $\mathcal{L}$ -PLDM

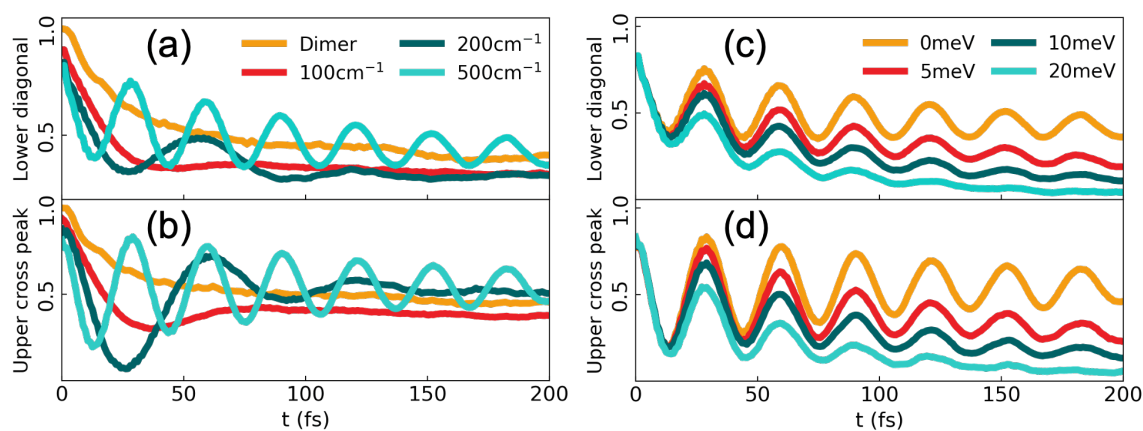


FIG. 8. (a) and (b) present the time-dependent 2DES signal intensity (along  $t_2$ ) in the upper diagonal peak and upper off-diagonal cross-peak of an exciton dimer coupled to the cavity at different light-matter coupling strength  $\hbar g_c$  for a lossless cavity ( $\Gamma = 0\text{meV}$ ). (c) and (d) present the time-dependent 2DSE signal intensity in the upper diagonal peak and the upper off-diagonal cross-peak intensity of a dimer coupled to the cavity with different cavity loss rate  $\Gamma$  for a fixed light-matter coupling strength  $\hbar g_c = 500\text{cm}^{-1}$ .

approach are in excellent agreement with the analytic answer (Eq. 57), at various light-matter coupling strengths and cavity loss rates. In particular, with an increasing cavity loss rate, we observe a decrease in Rabi splitting, which can be attributed to an effective decrease in light-matter coupling strength due to the difference between the cavity and matter line widths.

We then present the results of the pure absorptive 2D spectra for the monomer coupling to the cavity when varying cavity loss rates and light-matter coupling strengths. In the off-diagonal peaks (cross peaks) of the polariton 2D spectra, we observe the coherent energy exchange between the upper and lower polariton states, with the frequency corresponding to the Rabi splitting. Further, the cavity loss acts as a homogeneous broadening (width along the anti-diagonal direction of the diagonal peaks in Fig. 5) that dampens the polaritonic energy transfer and signal intensities. The increase in light-matter coupling strength causes a larger splitting of polaritonic peaks. Finally, we present the 2D spectra of an exciton dimer coupled to a cavity. We present the total signal for the 2D spectra as well as individual contributions from different Liouville pathways, including ground state bleaching (GSB), stimulated emission (SE), and excited state absorption (ES), for both rephasing and non-rephasing pathways. These pathways are then interpreted from how different polariton eigenstates contribute to each of the signals on the basis of the dipole matrix in the polariton eigenbasis.

In the 2D spectra of the dimer coupled to the cavity, we further observe a significant increase in polariton coherence time with increased cavity coupling strength, compared to the excitonic coherence time for the system outside the cavity. At room temperature with a cavity loss rate of  $\Gamma = 10\text{meV}$ , the coherence lifetime of a molecular dimer can be significantly prolonged up to 200

fs (from  $< 50\text{fs}$  outside the cavity), with a light-matter coupling strength of  $\Omega_R \approx 124\text{meV}$ . The prolonged off-diagonal oscillations are the direct consequence of the polaron decoupling effect<sup>6,7,9</sup> where the light-matter coupling effectively decreases the exciton-phonon coupling of the system (see Eq. 46), leading to a longer polariton coherence time. This is a clear theoretical demonstration of the polaron decoupling effect by simulating the polariton 2DES spectra. Similar experimental conditions for  $\Gamma$  and  $\Omega_R$  have been recently achieved when coupling CdSe nanoplatelets to a dielectric optical cavity,<sup>48</sup> and we envision observing such an effect from direct experimental measurements in the future.

## ACKNOWLEDGMENTS

This work was supported by the Department of Energy under Grant No. DE-SC0022171. P.H. appreciates the support from his Cottrell Scholar Award (a program by the Research Corporation for Science Advancement). Computing resources were provided by the Center for Integrated Research Computing (CIRC) at the University of Rochester. The authors appreciate valuable discussions and comments from Arkajit Mandal, Benjamin Chng, and Aamod Atre.

## CONFLICT OF INTEREST

The authors have no conflicts to disclose.

## AVAILABILITY OF DATA

The data that support the findings of this work are available from the corresponding author under reasonable request.

## Appendix A: Derivation of the $\mathcal{L}$ -PLDM approach

We provide a brief derivation of the  $\mathcal{L}$ -PLDM method (Eq. 27) described in Sec. II C (see similar discussions for the Ehrenfest dynamics in Ref. 47 for details). The decay dynamics of the reduced density matrix elements in the subspace of  $\{|0\rangle, |1\rangle\}$ , governed by the jump operator  $\hat{L} = |0\rangle\langle 1|$  are expressed (based on Eq. 19) as follows

$$\rho_{11}(t + dt) = e^{-\Gamma dt} \rho_{11}(t), \quad (\text{A1a})$$

$$\rho_{00}(t + dt) = \rho_{00}(t) + (1 - e^{-\Gamma dt}) \rho_{11}(t), \quad (\text{A1b})$$

$$\rho_{01}(t + dt) = e^{-\Gamma dt/2} \rho_{01}(t), \quad (\text{A1c})$$

$$\rho_{10}(t + dt) = e^{-\Gamma dt/2} \rho_{10}(t). \quad (\text{A1d})$$

Further, for the coherences that involve states  $|j\rangle \notin \{|0\rangle, |1\rangle\}$  due to the influence of the jump operator  $\hat{L}$ , the following equations hold

$$\rho_{j1}(t + dt) = e^{-\Gamma dt/2} \rho_{j1}(t), \quad (\text{A2a})$$

$$\rho_{1j}(t + dt) = e^{-\Gamma dt/2} \rho_{1j}(t), \quad (\text{A2b})$$

$$\rho_{j0}(t + dt) = \rho_{j0}(t), \quad (\text{A2c})$$

$$\rho_{0j}(t + dt) = \rho_{0j}(t). \quad (\text{A2d})$$

The joint probability distribution of complex random variables that update the PLDM coefficients must satisfy Eq. 26. For the variables  $\eta_{1,\xi}^F$  and  $\eta_{1,\xi}^B$  in Eq. 24, the following expectation values must hold

$$\langle \eta_{1,\xi}^F \eta_{1,\xi}^{B*} \rangle = e^{-\Gamma dt}, \quad (\text{A3})$$

in order to satisfy Eq. A1a. Further, to satisfy Eq. A2a-A2b, the following relation is required

$$\langle \eta_{1,\xi}^F \rangle = \langle \eta_{1,\xi}^B \rangle = e^{-\Gamma dt/2}. \quad (\text{A4})$$

The simple choice of  $\eta_{1,\xi}^F = \eta_{1,\xi}^B = e^{-\Gamma dt/2}$  satisfies Eq. A3 and Eq. A4. Note that this is just one possible choice of many possible choices. The variables  $\eta_{0,\xi}^F$  and  $\eta_{0,\xi}^B$  must satisfy a different set of expectation values. In particular, to satisfy Eq. A2c-A2d, we have

$$\langle \eta_{0,\xi}^F \rangle = \langle \eta_{0,\xi}^B \rangle = 1, \quad (\text{A5})$$

and to satisfy Eq. A1b, we have

$$\langle \eta_{0,\xi}^F \eta_{0,\xi}^{B*} \rangle = 1 + (1 - e^{-\Gamma dt}) \frac{\mathcal{Z}_{1,\xi}^F(t) \mathcal{Z}_{1,\xi}^{B*}(t)}{\mathcal{Z}_{0,\xi}^F(t) \mathcal{Z}_{0,\xi}^{B*}(t)}, \quad (\text{A6})$$

Note that the assumption that  $\eta_{0,\xi}^F = \eta_{0,\xi}^B$  will not work because the left-hand side of Eq. A6 would be a purely

real number (which corresponds to the population of state  $|0\rangle$ ) while the right-hand side of Eq. A6 is complex in the general case. Likewise,  $\eta_{0,\xi}^F$  and  $\eta_{0,\xi}^B$  cannot be independent random variables since this would imply  $\langle \eta_{0,\xi}^F \eta_{0,\xi}^{B*} \rangle = \langle \eta_{0,\xi}^F \rangle \langle \eta_{0,\xi}^{B*} \rangle = 1$ , which cannot satisfy the right-hand side of Eq. A6. Instead, we make the *ansatz* that  $\eta_{0,\xi}^F = \eta_{0,\xi}^{B*}$  which when applied to Eq. A5 and Eq. A6 leads to the following expectation value equations

$$\langle \eta_{0,\xi}^F \rangle = 1, \quad (\text{A7a})$$

$$\langle (\eta_{0,\xi}^F)^2 \rangle = 1 + (1 - e^{-\Gamma dt}) \frac{\mathcal{Z}_{1,\xi}^F(t) \mathcal{Z}_{1,\xi}^{B*}(t)}{\mathcal{Z}_{0,\xi}^F(t) \mathcal{Z}_{0,\xi}^{B*}(t)}. \quad (\text{A7b})$$

Equations A7a and A7b describe the first and second moments, respectively, of the probability distribution of  $\eta_{0,\xi}^F$ . These can be used to describe the pseudo-variance,  $\text{PVar}$ , of the probability distribution (note that the variance of a complex number is always a non-negative real number while the pseudo-variance is complex in general). The pseudo-variance of  $\eta_{0,\xi}^F$  is

$$\begin{aligned} \text{PVar}(\eta_{0,\xi}^F) &= \langle (\eta_{0,\xi}^F)^2 \rangle - \langle \eta_{0,\xi}^F \rangle^2, \quad (\text{A8}) \\ &= (1 - e^{-\Gamma dt}) \frac{\mathcal{Z}_{1,\xi}^F(t) \mathcal{Z}_{1,\xi}^{B*}(t)}{\mathcal{Z}_{0,\xi}^F(t) \mathcal{Z}_{0,\xi}^{B*}(t)}. \end{aligned}$$

Note that  $(\eta_{0,\xi}^F)^2$  is a complex number (not to be confused with  $|\eta_{0,\xi}^F|^2 = \eta_{0,\xi}^F \eta_{0,\xi}^{F*}$  which is a real number). The probability distribution of  $\eta_{0,\xi}^F$  can thus be chosen as any distribution with mean 1 (see Eq. A7a) and pseudo-variance given in Eq. A8. We choose a uniform distribution corresponding to a line segment in the complex plane with mean 1 and complex boundaries that give the correct pseudo-variance. For convenience, a complex random number  $z$  with a uniform distribution on a line segment in the complex plane can be written in terms of a standard uniform random variable  $r \in [0, 1]$  as  $z = \langle z \rangle + (2r - 1) \sqrt{3 \cdot \text{PVar}(z)}$ . Thus,  $\eta_{0,\xi}^F$  can be written as

$$\eta_{0,\xi}^F = 1 + (2r - 1) \sqrt{3(1 - e^{-\Gamma dt}) \frac{\mathcal{Z}_{1,\xi}^F(t) \mathcal{Z}_{1,\xi}^{B*}(t)}{\mathcal{Z}_{0,\xi}^F(t) \mathcal{Z}_{0,\xi}^{B*}(t)}}, \quad (\text{A9})$$

with a uniform real random number  $r \in [0, 1]$ . Furthermore,  $\eta_{0,\xi}^B = \eta_{0,\xi}^{F*}$  due to the *ansatz*.

Note that the random variables  $\eta_{1,\xi}^F$  and  $\eta_{0,\xi}^F$  must also satisfy Eq. A1c and Eq. A1d, which correspond to

$$\langle \eta_{1,\xi}^F \eta_{0,\xi}^{B*} \rangle = e^{-\Gamma dt/2}. \quad (\text{A10})$$

The above relations are automatically satisfied by the chosen distributions of  $\eta_{1,\xi}^F$  and  $\eta_{0,\xi}^F$  since  $\langle \eta_{1,\xi}^F \eta_{0,\xi}^{B*} \rangle = e^{-\Gamma dt/2} \langle \eta_{0,\xi}^{B*} \rangle = e^{-\Gamma dt/2}$ .

## Appendix B: Direct comparison between the Lindblad and the $\mathcal{L}$ -PLDM approach

Here, we present a direct comparison of the original Lindblad dynamics (Eq. 18) and the stochastic method (Eq. 27). The model used in Fig. 9 includes the monomer-cavity Hamiltonian with  $\hat{H}_R = \hat{H}_{\text{ex-R}} = 0$ , a cavity loss rate of  $\Gamma = 10$  meV and a coupling strength of  $\hbar g_c = 456$   $\text{cm}^{-1}$ . Fig. 9a presents the population dynamics of the exciton-photon basis, with the initial state  $|g1\rangle\langle g1|$ . The results obtained from the exact Lindblad dynamics simulation (Eq. 18) are depicted by solid lines. The  $\mathcal{L}$ -PLDM dynamics (dotted lines) exactly reproduce the Lindblad simulations, with  $10^4$  trajectories.

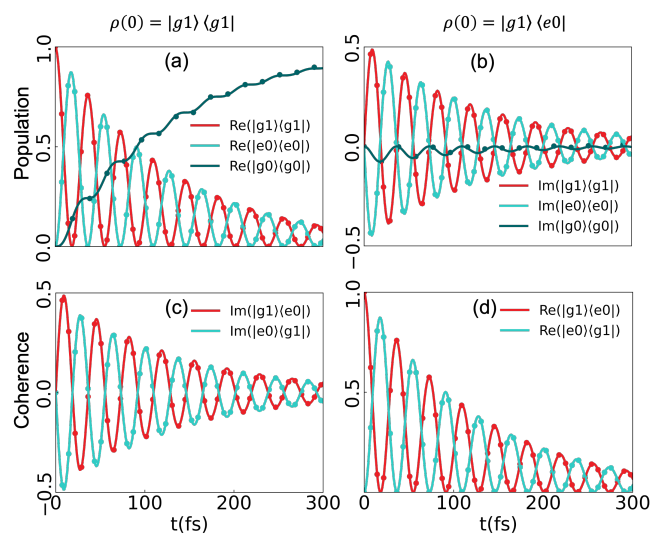


FIG. 9. Density matrix dynamics comparison of Lindblad (solid line) with  $\mathcal{L}$ -PLDM (dotted) dynamics.

Fig. 9b presents the dynamics with the initial condition starting from a non-Hermitian density matrix  $|g1\rangle\langle e0|$ , which is the necessary component for simulating optical response functions. Because of the asymmetry of the coherence elements in the initial density matrix, we see the rise of imaginary populations. Here, we can see the coherent transfer between the  $|g1\rangle$ ,  $|e0\rangle$ , and  $|g0\rangle$  states and the decay of all magnitudes due to loss.

Fig. 9c presents the dynamics of coherence matrix elements between  $|g1\rangle$  and  $|e0\rangle$  states when we started with  $|g1\rangle\langle g1|$ . With time, we see the decay of coherence exchange between the states. Fig. 9d presents the evolution of coherence elements when the dynamics start with  $|g1\rangle\langle e0|$ . This represents the decoherence process due to cavity loss. In all the cases presented in Fig. 9, one can clearly see that the  $\mathcal{L}$ -PLDM dynamics (dotted lines) quantitatively reproduce the original Lindblad results.

Having compared the density matrix dynamics, we now focus on comparing the purely absorptive 2DES results (without the phonon dynamics by setting  $\hat{H}_R = \hat{H}_{\text{ex-R}} = 0$ ). We use the same model as in Fig. 9 and compare the

2DES for two different cavity loss rates in Fig. 10 ( $\Gamma = 10$  meV) and Fig. 11 ( $\Gamma = 50$  meV), both generated with  $10^5$  trajectories. The  $\mathcal{L}$ -PLDM generates 2DES with visually identical results compared to the Lindblad dynamics.

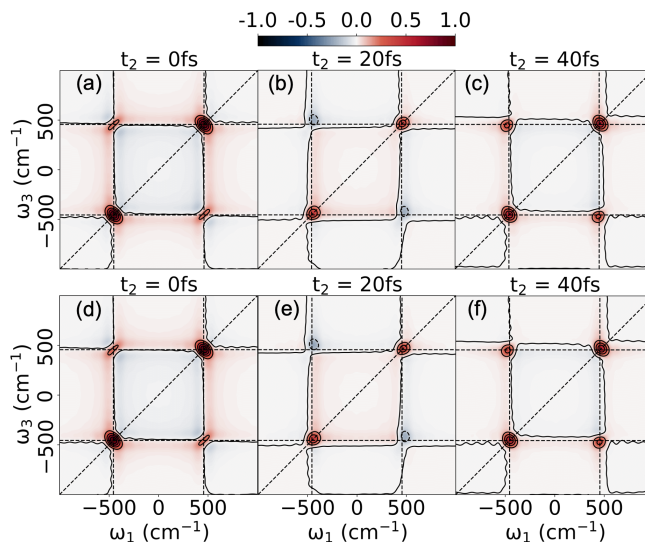


FIG. 10. 2DES spectra of an exciton monomer coupled to the cavity, by setting exciton-phonon coupling to be zero  $\hat{H}_R + \hat{H}_{\text{ex-R}} = 0$ . The light-matter coupling strength is  $\hbar g_c = 500$   $\text{cm}^{-1}$ , and the cavity loss rate is  $\Gamma = 10$  meV. The spectra are calculated with (a)-(e) the original Lindblad approach (Eq. 19) and (d)-(f)  $\mathcal{L}$ -PLDM dynamics (Eq. 28).

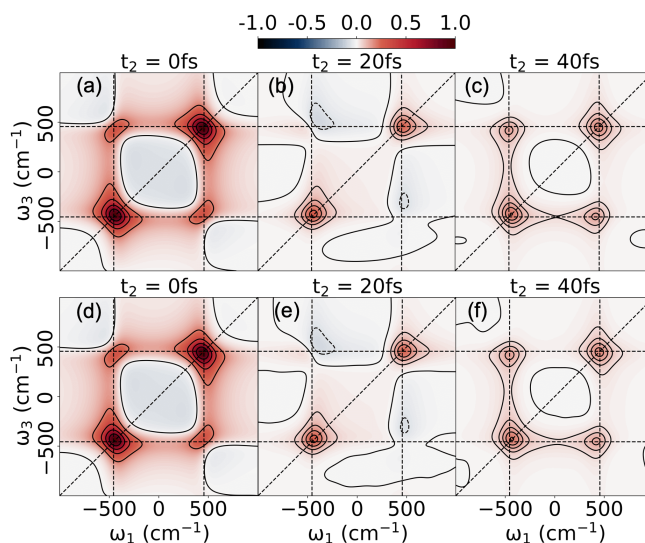


FIG. 11. 2DES spectra of a monomer coupled to the cavity. Same model parameters are used as in Fig. 10, except for the cavity loss rate  $\Gamma = 50$  meV. The spectra are calculated with (a)-(e) Lindblad and (d)-(f)  $\mathcal{L}$ -PLDM dynamics.

<sup>1</sup>J. A. Hutchison, T. Schwartz, C. Genet, E. Devaux, and T. W. Ebbesen, “Modifying chemical landscapes by coupling to vacuum fields,” *Angew. Chem. Int. Ed.* **51**, 1592–1596 (2012).



- <sup>2</sup>T. Schwartz, J. A. Hutchison, C. Genet, and T. W. Ebbesen, “Reversible switching of ultrastrong light-molecule coupling,” *Phys. Rev. Lett.* **106**, 196405 (2011).
- <sup>3</sup>B. Munkhbat, M. Wersäll, D. G. Baranov, T. J. Antosiewicz, and T. Shegai, “Suppression of photo-oxidation of organic chromophores by strong coupling to plasmonic nanoantennas,” *Sci. Adv.* **4**, eaas9552 (2018).
- <sup>4</sup>K. Stranius, M. Hertzog, and K. Börjesson, “Selective manipulation of electronically excited states through strong light-matter interactions,” *Nat. Commun.* **9**, 1–7 (2018).
- <sup>5</sup>T. W. Ebbesen, “Hybrid light-matter states in a molecular and material science perspective,” *Acc. Chem. Res.* **49**, 2403–2412 (2016).
- <sup>6</sup>F. Herrera and F. C. Spano, “Cavity-controlled chemistry in molecular ensembles,” *Phys. Rev. Lett.* **116**, 238301 (2016).
- <sup>7</sup>F. Herrera and F. C. Spano, “Theory of nanoscale organic cavities: The essential role of vibration-photon dressed states,” *ACS Photonics* **5**, 65–79 (2018).
- <sup>8</sup>F. Herrera and F. C. Spano, “Absorption and photoluminescence in organic cavity qed,” *Phys. Rev. A: At. Mol. Opt. Phys.* **95**, 053867 (2017).
- <sup>9</sup>S. Takahashi and K. Watanabe, “Decoupling from a thermal bath via molecular polariton formation,” *J. Phys. Chem. Lett.* **11**, 1349–1356 (2020).
- <sup>10</sup>D. Xu, A. Mandal, J. M. Baxter, S.-W. Cheng, I. Lee, H. Su, S. Liu, D. R. Reichman, and M. Delor, “Ultrafast imaging of coherent polariton propagation and interactions,” *arXiv preprint arXiv:2205.01176* (2022).
- <sup>11</sup>R. Pandya, A. Ashoka, K. Georgiou, J. Sung, R. Jayaprakash, S. Renken, L. Gai, Z. Shen, A. Rao, and A. J. Musser, “Tuning the coherent propagation of organic exciton-polaritons through dark state delocalization,” *Advanced Science* **9**, 2105569 (2022).
- <sup>12</sup>M. Balasubrahmaniam, A. Simkhovich, A. Golombek, G. Sandik, G. Ankonina, and T. Schwartz, “From enhanced diffusion to ultrafast ballistic motion of hybrid light-matter excitations,” *Nature Materials* , 1–7 (2023).
- <sup>13</sup>A. G. Avramenko and A. S. Rury, “Local molecular probes of ultrafast relaxation channels in strongly coupled metalloporphyrin-cavity systems,” *The Journal of Chemical Physics* **155**, 064702 (2021).
- <sup>14</sup>T. M. Autry, G. Nardin, C. L. Smallwood, K. Silverman, D. Bajoni, A. Lemaître, S. Bouchoule, J. Bloch, and S. Cundiff, “Excitation ladder of cavity polaritons,” *Physical Review Letters* **125**, 067403 (2020).
- <sup>15</sup>H. Li, S. Shah, A. R. S. Kandada, C. Silva, A. Piryatinski, and E. R. Bittner, “The optical signatures of stochastic processes in many-body exciton scattering,” *Annual Review of Physical Chemistry* **74**, 467–492 (2023).
- <sup>16</sup>D. Cho, B. Gu, and S. Mukamel, “Optical cavity manipulation and nonlinear uv molecular spectroscopy of conical intersections in pyrazine,” *Journal of the American Chemical Society* **144**, 7758–7767 (2022).
- <sup>17</sup>D. Finkelstein-Shapiro, P.-A. Mante, S. Balci, D. Zigmantas, and T. Pullerits, “Non-hermitian hamiltonians for linear and nonlinear optical response: A model for plexcitons,” *J. Chem. Phys.* **158** (2023).
- <sup>18</sup>Z. Zhang, X. Nie, D. Lei, and S. Mukamel, “Multidimensional coherent spectroscopy of molecular polaritons: Langevin approach,” *Physical Review Letters* **130**, 103001 (2023).
- <sup>19</sup>J. Provazza, F. Segatta, M. Garavelli, and D. F. Coker, “Semi-classical path integral calculation of nonlinear optical spectroscopy,” *J. Chem. Theory Comput.* **14**, 856–866 (2018).
- <sup>20</sup>P. Huo and D. F. Coker, “Communication: Partial linearized density matrix dynamics for dissipative, non-adiabatic quantum evolution,” *J. Chem. Phys.* **135**, 201101 (2011).
- <sup>21</sup>P. Huo and D. F. Coker, “Semi-classical path integral non-adiabatic dynamics: a partial linearized classical mapping hamiltonian approach,” *Mol. Phys.* **110**, 1035–1052 (2012).
- <sup>22</sup>M. K. Lee, P. Huo, and D. F. Coker, “Semiclassical path integral dynamics: Photosynthetic energy transfer with realistic environment interactions,” *Annu. Rev. Phys. Chem.* **67**, 639–668 (2016).
- <sup>23</sup>S. Mukamel, *Principles of nonlinear optical spectroscopy*, 6 (Oxford University Press on Demand, 1999).
- <sup>24</sup>A. Gelzinis, R. Augulis, V. Butkus, B. Robert, and L. Valkunas, “Two-dimensional spectroscopy for non-specialists,” *Biochim. Biophys. Acta, Bioenerg.* **1860**, 271–285 (2019).
- <sup>25</sup>S. Biswas, J. Kim, X. Zhang, and G. D. Scholes, “Coherent two-dimensional and broadband electronic spectroscopies,” *Chem. Rev.* **122**, 4257–4321 (2022).
- <sup>26</sup>A. M. Brańczyk, D. B. Turner, and G. D. Scholes, “Crossing disciplines—a view on two-dimensional optical spectroscopy,” *Ann. Phys.* **526**, 31–49 (2014).
- <sup>27</sup>E. Collini, “2d electronic spectroscopic techniques for quantum technology applications,” *J. Phys. Chem. C* **125**, 13096–13108 (2021).
- <sup>28</sup>P. Hamm, “Principles of nonlinear optical spectroscopy: A practical approach or: Mukamel for dummies,” *University of Zurich* **41**, 77 (2005).
- <sup>29</sup>M. Cho, *Two-dimensional optical spectroscopy* (CRC press, 2009).
- <sup>30</sup>L. Valkunas, D. Abramavicius, and T. Mancal, *Molecular excitation dynamics and relaxation: quantum theory and spectroscopy* (John Wiley & Sons, 2013).
- <sup>31</sup>Y. Tanimura, “Numerically “exact” approach to open quantum dynamics: The hierarchical equations of motion (heom),” *J. Chem. Phys.* **153**, 020901 (2020).
- <sup>32</sup>T. Kramer, M. Noack, A. Reinefeld, M. Rodríguez, and Y. Zelinskyy, “Efficient calculation of open quantum system dynamics and time-resolved spectroscopy with distributed memory heom (dm-heom),” *J. Comput. Chem.* **39**, 1779–1794 (2018).
- <sup>33</sup>R. F. Loring, “Calculating multidimensional optical spectra from classical trajectories,” *Annu. Rev. Phys. Chem.* **73**, 273–297 (2022).
- <sup>34</sup>J. R. Mannouch and J. O. Richardson, “A partially linearized spin-mapping approach for simulating nonlinear optical spectra,” *J. Chem. Phys.* **156**, 024108 (2022).
- <sup>35</sup>A. O. Atsango, A. Montoya-Castillo, and T. E. Markland, “An accurate and efficient ehrenfest dynamics approach for calculating linear and nonlinear electronic spectra,” *J. Chem. Phys.* **158** (2023).
- <sup>36</sup>C. Van Der Vegte, A. Dijkstra, J. Knoester, and T. Jansen, “Calculating two-dimensional spectra with the mixed quantum-classical ehrenfest method,” *J. Phys. Chem. A* **117**, 5970–5980 (2013).
- <sup>37</sup>R. Tempelaar, C. P. Van Der Vegte, J. Knoester, and T. L. Jansen, “Surface hopping modeling of two-dimensional spectra,” *J. Chem. Phys.* **138**, 164106 (2013).
- <sup>38</sup>S. Chaturvedi and F. Shibata, “Time-convolutionless projection operator formalism for elimination of fast variables. applications to brownian motion,” *Z. Phys. B: Condens. Matter Quanta* **35**, 297–308 (1979).
- <sup>39</sup>F. Shibata, Y. Takahashi, and N. Hashitsume, “A generalized stochastic liouville equation. non-markovian versus memoryless master equations,” *J. Stat. Phys.* **17**, 171–187 (1977).
- <sup>40</sup>J. H. Fetherolf and T. C. Berkelbach, “Linear and nonlinear spectroscopy from quantum master equations,” *J. Chem. Phys.* **147**, 244109 (2017).
- <sup>41</sup>A. Ishizaki and Y. Tanimura, “Nonperturbative non-markovian quantum master equation: Validity and limitation to calculate nonlinear response functions,” *Chem. Phys.* **347**, 185–193 (2008).
- <sup>42</sup>S. Mukamel, Y. Tanimura, and P. Hamm, “Coherent multidimensional optical spectroscopy,” (2009).
- <sup>43</sup>H.-D. Meyer and W. H. Miller, “A classical analog for electronic degrees of freedom in nonadiabatic collision processes,” *J. Chem. Phys.* **70**, 3214–3223 (1979).
- <sup>44</sup>G. Stock and M. Thoss, “Semiclassical description of nonadiabatic quantum dynamics,” *Phys. Rev. Lett.* **78**, 578 (1997).
- <sup>45</sup>M. Thoss and G. Stock, “Mapping approach to the semiclassical description of nonadiabatic quantum dynamics,” *Phys Rev A* **59**, 64 (1999).

- <sup>46</sup>P. Huo and D. F. Coker, “Consistent schemes for non-adiabatic dynamics derived from partial linearized density matrix propagation,” *J. Chem. Phys.* **137**, 22A535 (2012).
- <sup>47</sup>E. R. Koessler, A. Mandal, and P. Huo, “Incorporating lindblad decay dynamics into mixed quantum-classical simulations,” *J. Chem. Phys.* **157**, 064101 (2022).
- <sup>48</sup>L. Qiu, A. Mandal, O. Morshed, M. T. Meidenbauer, W. Girten, P. Huo, A. N. Vamivakas, and T. D. Krauss, “Molecular polaritons generated from strong coupling between CdSe nanoplatelets and a dielectric optical cavity,” *J. Phys. Chem. Lett.* **12**, 5030–5038 (2021).
- <sup>49</sup>B. M. Weight, T. D. Krauss, and P. Huo, “Investigating molecular exciton polaritons using ab initio cavity quantum electrodynamics,” *J. Phys. Chem. Lett.* **14**, 5901–5913 (2023).
- <sup>50</sup>J. Torres-Sánchez and J. Feist, “Molecular photodissociation enabled by ultrafast plasmon decay,” *J. Chem. Phys.* **154**, 014303 (2021).
- <sup>51</sup>P. L. Walters, T. C. Allen, and N. Makri, “Direct determination of discrete harmonic bath parameters from molecular dynamics simulations,” *J. Comput. Chem.* **38**, 110–115 (2017).
- <sup>52</sup>K. Müller, K. A. Fischer, A. Rundquist, C. Dory, K. G. Lagoudakis, T. Sarmiento, Y. A. Kelaita, V. Borish, and J. Vučković, “Ultrafast polariton-phonon dynamics of strongly coupled quantum dot-nanocavity systems,” *Physical Review X* **5**, 031006 (2015).
- <sup>53</sup>F. P. Laussy, E. del Valle, M. Schrapp, A. Laucht, and J. J. Finley, “Climbing the jaynes–cummings ladder by photon counting,” *J. Nanophoton.* **6**, 061803–061803 (2012).
- <sup>54</sup>A. Mandal, M. Taylor, B. Weight, E. Koessler, X. Li, and P. Huo, “Theoretical advances in polariton chemistry and molecular cavity quantum electrodynamics,” (2022).
- <sup>55</sup>V. Tiwari, W. K. Peters, and D. M. Jonas, “Electronic resonance with anticorrelated pigment vibrations drives photosynthetic energy transfer outside the adiabatic framework,” *Proceedings of the National Academy of Sciences* **110**, 1203–1208 (2013).
- <sup>56</sup>E. Thyrgaug, R. Tempelaar, M. J. Alcocer, K. Židek, D. Bina, J. Knoester, T. L. Jansen, and D. Zigmantas, “Identification and characterization of diverse coherences in the fenna–matthews–olson complex,” *Nature chemistry* **10**, 780–786 (2018).
- <sup>57</sup>A. Halpin, P. J. Johnson, R. Tempelaar, R. S. Murphy, J. Knoester, T. L. Jansen, and R. D. Miller, “Two-dimensional spectroscopy of a molecular dimer unveils the effects of vibronic coupling on exciton coherences,” *Nature chemistry* **6**, 196–201 (2014).